Methods for Detecting High-Frequency Oscillations in Ongoing Brain Signals: Application to the Determination of Epileptic Seizure Onset Zones

Chiran Dilip Doshi
Marquette University

METHODS FOR DETECTING HIGH-FREQUENCY OSCILLATIONS IN ONGOING BRAIN SIGNALS: APPLICATION TO THE DETERMINATION OF EPILEPTIC SEIZURE ONSET ZONES

by

Chiran D. Doshi, B.S.

A Thesis submitted to the Faculty of the Graduate School,
Marquette University,
in Partial Fulfillment of the Requirements for
the Degree of Master of Science

Milwaukee, Wisconsin

August 2011

ABSTRACT
METHODS FOR DETECTING HIGH-FREQUENCY OSCILLATIONS
IN ONGOING BRAIN SIGNALS: APPLICATION TO THE
DETERMINATION OF EPILEPTIC SEIZURE ONSET ZONES

Chiran D. Doshi, B.S.

Marquette University, 2011

Epilepsy is a neurological disorder with varied expression. Patients with focal onset seizures that are resistant to medications can benefit from ablative surgery. However, localization of the seizure onset zone (SOZ) and characterization of propagation to secondary areas can be challenging. The present study is aimed at developing appropriate signal processing methodology to detect bursts of interictal high-frequency oscillations (HFOs), as a possible signature of the SOZ, in patients with drug-resistant partial epilepsy. Invasive interictal and ictal intracranial electroencephalography (iEEG) data and non-invasive electromagnetic source imaging with magnetoencephalography (MEG) data from three subjects were analyzed. We developed a novel algorithm that extracts HFO bursts from the envelope of iEEG and MEG traces in the [80-300] Hz range. Clusters of HFO events were subsequently analyzed to investigate their relative time delays and to infer possible propagation patterns during the interictal period and episodes of ictal onset (iEEG only). The location of iEEG electrodes were labeled with respect to the chronometry of the detected HFOs. The recording site bearing the smallest rank was labeled as the lead generator of HFO discharges. The aim of using MEG traces was essentially to determine probable SOZ locations. We proposed a new metric referred to as 'spiking index' that was computed at each cortical site in the vicinity of iEEG electrode locations (iEEG and MEG data were obtained for the same patients: iEEG was considered as the standard of reference for MEG results). The sensitivity and specificity of the HFO detector operating from ongoing brain traces were evaluated. Our results indicate that higher values of spiking index and higher rates of HFOs corresponded to brain regions that were identified independently as the SOZ by an expert clinician and as determined by the location and extent of the cortical resection that freed the patients from the seizures. Interictal and ictal iEEG HFO localization showed good concordance with the location of resected areas.

The use of interictal data only, if used for surgical planning, would reduce the time required for making decisions regarding the resection of cortex and improve the chances of successful surgery. Obtaining iEEG data is invasive, with possible risks to the patients. Another fundamental disadvantage of iEEG is that the implanted electrode grids and strips needed to cover the supposed abnormal cortical areas for proper determination of the SOZ. Our results indicate that the spiking index and rate map obtained from MEG source maps may provide a non-invasive alternative for determination of the SOZ and may provide greater accuracy to the placement of the implantable electrodes, and eventually avoid an invasive exploratory procedure before surgery.

ACKNOWLEDGMENTS

Chiran D. Doshi, B.S.

I would like to acknowledge my funding source, The Falk Medical Research Trust, Marquette University and the Medical College of Wisconsin. This study was conducted at the MEG lab in the department of Neurology at the Froedtert Hospital and the Medical College of Wisconsin.

Dr. Sylvain Baillet has been truly instrumental in shaping my project as well as my career and I would like to thank him for his important inputs and feedback. The knowledge and experience that I gained at his lab would always hold steady in the years to come. I would also like to thank, Dr. Manoj Raghavan for providing me with the data as well as valuable ideas for the project. The talks about epilepsy with him and Dr. Baillet really got me motivated. I would like to acknowledge, Peter LaViolette for providing the structural data of the subjects that were used extensively in the analysis.

I would like to thank, Dr. Kristina Ropella for providing her valuable inputs, guiding support and the encouragement to always perform better. I would also like to thank, Dr. Scott Beardsley for teaching me a lot of things about Matlab, research and also for serving on my thesis committee.

I have been fortunate to work with Dr. Rey Ramirez and Elizabeth Bock who have been my colleagues and mentors. I would also like to thank my roommates and friends, Sanket Jain and Tushar Navale for being a wonderful support.

I would like to dedicate this thesis to my family and friends who have always put faith in my abilities and have inspired me to reach greater heights throughout my career.

TABLE OF CONTENTS

LIST OF TABLES

LIST OF FIGURES

1 INTRODUCTION AND LITERATURE REVIEW

1.1 Brain Anatomy and Physiology

The brain along with the spinal cord constitutes the central nervous system (CNS). The brain is one of the most complex organs and in spite of decades of research, it continues to both amaze and confuse us. The brain is the center for sensory, motor, visual, auditory and olfactory systems, and it is also the center responsible for emotional behavior and cognition. The adult human brain weighs about 3 lbs (Parent et al., 1995). It is covered by membranes, cerebrospinal fluid (CSF) and bones. The complexity of the brain lies essentially in the convoluted cerebral cortex consisting of about 10^{11} neurons, with 10^{15} synaptic connections (Murre et al., 1995).

The neurons form the building blocks of the nervous system. They specialize in receiving and transmitting information by means of chemical and electrical signals. They consist of a cell body (soma), dendrites and an axon (Figure 1.1). The dendrites are branched projections that arise from the soma. They consist of dendritic spines that receive inputs from the axon of other connected neurons. The axons are responsible for carrying action potentials that excite or inhibit connected neurons, muscles or glands. They generally branch and their distal terminations are known as the axon terminal. The junction between the axon and the dendrite is called a synapse, which is an essential component of neural communication. In a chemical synapse, the pre-synaptic neuron releases a neurotransmitter in the synaptic cleft that binds to the receptors of the postsynaptic cell. Depending on the type of neurotransmitter released and the receptor properties, the effect on the postsynaptic cell is either excitatory or inhibitory.

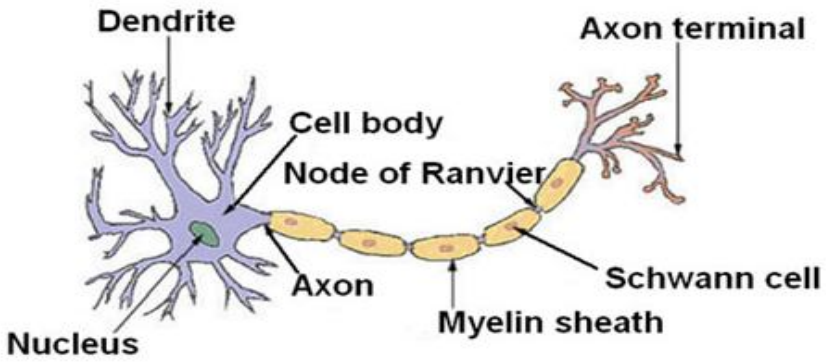

Figure 1 Structure of a neuron. The neuron consists of essentially three main components: the dendrites, soma and the axon. Adapted from http://psychology.wikia.com/wiki/Brain

The brain consists of different parts that are integrated to work as a unit: the brain stem, the cerebellum, the diencephalon and the cerebrum (Figure 1.2). The brainstem consists of the medulla oblongata, the pons varolli, and the midbrain. The medulla is responsible for autonomic functions like breathing and regulation of blood pressure. It also contains the cardiac, respiratory, vomiting and vasomotor centers. The pons connects the cerebellum to the rest of the brain and along with the medulla, regulates breathing (Saladin, 2007). The midbrain acts as a relay station for auditory and visual information. Portions of the midbrain are involved in the regulation of body movements. The cerebellum helps in coordinating movements, maintaining posture and equilibrium in the body. The diencephalon consists of the hypothalamus, the thalamus and the epithalamus. The hypothalamus helps regulating the body temperature and produces important hormones like oxytocin and growth-hormone releasing hormone. The thalamus is involved in important regulatory functions of the cortical dynamics. Further, it's a central relay to sensory inputs (except for olfactory information). The cerebrum is the largest part

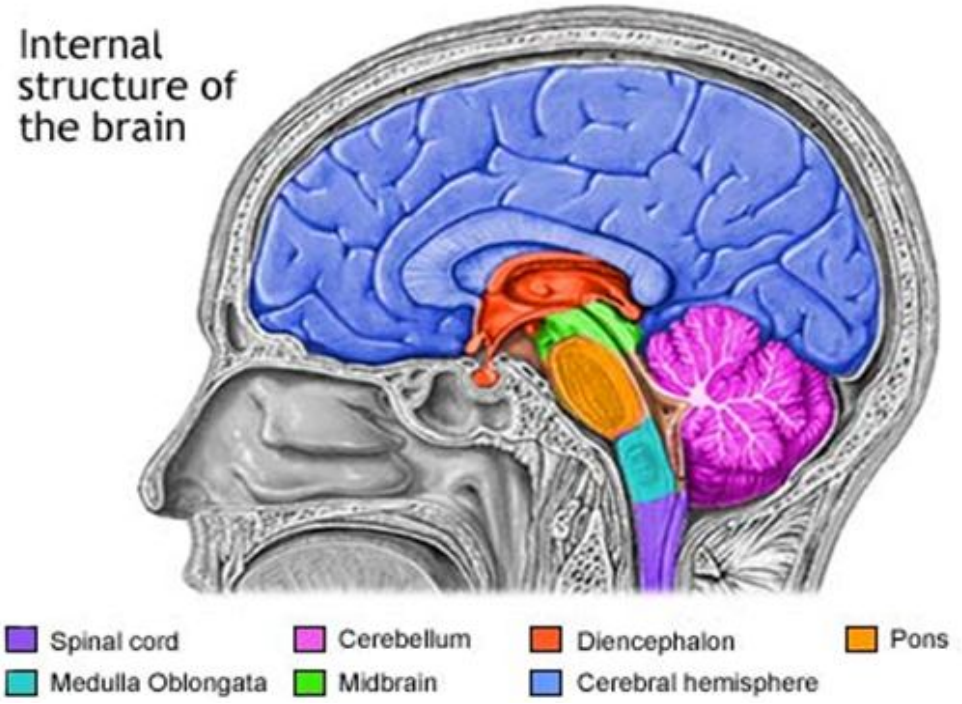

Figure 1.2 Internal structure of the brain. The colored regions of the brain are appropriately labeled. Adapted from http://pennstatehershey.adam.com

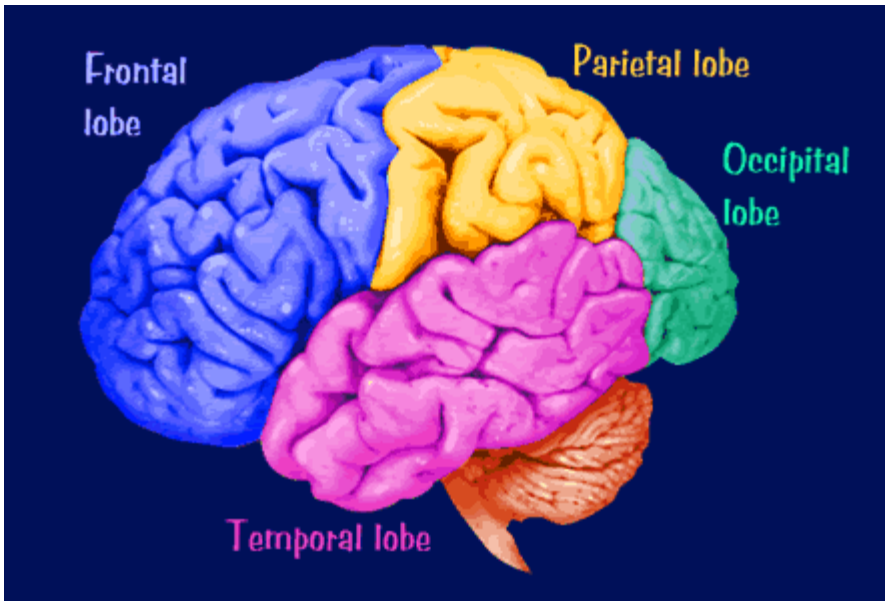

Figure 1.3 Structure of the cerebral cortex. The cerebral cortex can be divided broadly into four regions; the frontal lobe, the parietal lobe, the temporal lobe and the occipital lobe. Adapted from www.morphonix.com

of the brain. It is divided into cerebral hemispheres as defined on both sides of the longitudinal fissure. The outer surface of the cerebrum is known as the cerebral cortex. It is 1 to 4.5 mm thick (von Economo, 1929) (Figure 1.3) and highly convoluted. Connectivity between cortical neurons contributes to the complexity and diversity in the functions of the nervous system. The cerebral cortex, based on topography, can be broadly divided into the frontal, parietal, temporal and occipital lobes. The frontal lobe is located at the anterior part of each cerebral hemisphere. It is anterior to the parietal lobe and superior to the temporal lobe. The frontal lobe contains the motor areas of the brain and is involved in reasoning, planning and is also a center for emotions (Stuss et al., 1992). The left frontal lobe controls movements of the right side of the body and vice-versa. The parietal lobe lies posterior to the frontal lobe and is separated from the frontal lobe by the central sulcus. The parietal lobe contains the sensory areas which receive impulses related to temperature, touch, pain and pressure (Blakemore and Frith, 2005). The parietal lobe is involved in interpreting the spatial orientation of the body. The right parietal lobe receives sensations from the left side of the body and vice versa. The temporal lobe is located beneath the Sylvian fissure on both hemispheres. The primary auditory centers reside bilaterally in the temporal lobe about the posterior aspect of the Sylvian fissure. The occipital lobe lies inferior to the parietal and the temporal lobe. The primary visual cortex resides in the occipital lobe. Another structure worth mentioning is the hippocampus, which belongs to a set of sub-cortical regions called the limbic system. The hippocampus is located on the mesial aspects of the temporal lobe. It plays a major role in memory encoding/retrieval and in spatial navigation.

1.2 Understanding Epilepsy

Epilepsy is a neurological disorder characterized by recurrent unprovoked seizures. An epileptic seizure is an episode of disorganized electrical activity, typically related to excessive neuronal excitation in the cortex, with a broad range of symptoms, including loss of consciousness, involuntary movements, etc. A person who has experienced only one seizure cannot be qualified as being epileptic, since a healthy brain can be provoked into a seizure under various stresses. Epileptic seizures are unpredictable and may sometimes be resistant to antiepileptic medications, with consequent progressive neurological and cognitive dysfunction. Electrical changes in the brain related to seizures, often referred to as the ictal state, and typically last from seconds to minutes, but in some instances prolonged seizure activity or a succession of seizures result in a life-threatening condition called status epilpticus. The period between seizures is referred to as the interictal state. There are various types of seizures, which determine the therapy that the patient receives. Seizures are typically characterized as either generalized or partial. Generalized seizures involve the entire brain, whereas partial seizures are restricted to certain areas, although they may secondarily generalize or spread to other distant brain regions (complex partial seizure) or remain very focal with no compromise of awareness (simple partial seizure). Table 1.1 and 1.2 illustrate the different types of generalized and partial seizures and their common symptoms. If the underlying cause of the seizures is known (tumor, trauma etc.), the epilepsy is termed as symptomatic. If the cause of seizures is unknown (CT or MRI are normal), the epilepsy is termed as idiopathic. Seizures of the temporal lobe usually induce drastic changes to cognitive processes of an individual. Epilepsy of the temporal lobe can cause changes in moods and behavior

Generalized seizures	Symptoms
Generalized tonic clonic or "grand mal"	Loss of consciousness, stiffing of muscles followed by jerking movements, biting of tongue, confusion lasts for some amount of time after seizure
Absence or "petit mal"	Loss of consciousness, blank outs, no confusion after seizure
Myoclonic	Brief sporadic jerking of muscles
Clonic	Rhythmic jerking of muscles
Tonic	Stiffening of muscles, loss of balance
Atonic	Lapse of muscle tone resulting in loss of balance

Table 1.1: Types of generalized seizures and their symptoms

Partial seizures	Symptoms
Simple (person remains alert) a) Simple motor b) Simple sensory c) Simple psychological	 a) Jerking of muscles, rigidity b) Visual, hearing, touch or smell sensations are affected c) Déjà vu, unreasonable fear
Complex (awareness is impaired)	Loss of awareness but no convulsion followed by period of confusion
Secondarily generalized	Produces convulsion

Table 1.2: Types of partial seizures with their symptoms.

(Blumer & Beson, 1975). The temporal lobe is one of the brain regions that are commonly involved in partial epileptic networks. Abnormal oscillations recorded from the hippocampus are assumed to play an important role in some epileptic syndromes (Ibarz et al., 2010). The treatment of epilepsy involves the use of a palette of antiepileptic drugs (AEDs), as a first step. Medications generally work well in about 50% of the patients. These patients may remain seizure free if they strictly follow the medication regimen. In 20% of the cases, the frequency of seizures decreases greatly. About 30% of

the patients continue to experience seizures (intractable) in spite of AEDs (Cramer et al., 1999, Kwan et al., 2000). Neurosurgery for the resection of the seizure onset zone (SOZ) may a viable option in some cases.

1.3 Techniques for Monitoring the Epileptic Brain

1.3.1 Electroencephalography (EEG) and Intracranial EEG (iEEG)

Electroencephalography (EEG) consists in recording the electrical activity produced by the firing of an ensemble of neurons by means of electrodes attached to the scalp (Niedermeyer et. al., 2004). Richard Caton was the first to present his findings on sensory evoked responses in 1875. He observed continuous spontaneous electrical activity from exposed cerebral hemispheres of rabbits and monkeys (Swartz et. al., 1998). Hans Berger recorded the first human EEG in 1924 and coined the term '*Elektenkephalogram*' (Haas, 2003). EEG commonly refers to scalp EEG. Scalp EEG provides a poor spatial resolution of the cerebral location generating the scalp signals because of the smearing of neural electrical potentials introduced by the meninges, CSF and skull bone. Stereotactic EEG (SEEG) and intracranial EEG (iEEG) provide solutions to some of the limitations of scalp EEG. SEEG records neural electrical potentials from depth electrodes (reaching potentially deeper and sub-cortical brain regions) consisting of 1-D linear electrode arrays shaped in the form of a needle (Kahane et al., 2006). IEEG or electrocorticography (ECoG) consist of 2-D grids or 1-D strips placed directly on the cortical surface or the dura. In the context of epilepsy, iEEG and SEEG are essentially a two-step procedure. The first step involves a procedure to identify the epileptogenic

area(s) by means of placements of subdural electrodes (Luders et al., 1992, Behrens et al., 1994, De Salles et al., 1994, Adelson et al., 2005); if successful, the second procedure involves resection of the epileptogenic area (Quesney et al., 1995, Wennberg et al., 1998). Both recording techniques provide better spatial and temporal resolution and are considered as more indicative of the location of pathological cortical generators than scalp EEG. Indeed, the distortions of the EEG scalp potentials produced by the interface skull-scalp surface are avoided (Pfurtscheller and Cooper, 1975). Further, iEEG and SEEG are not contaminated by the artifacts caused by muscle activity, eye movements and eye blinks (Pfurtscheller & Cooper, 1975, Lachaux et al., 2003). The main disadvantage of SEEG and iEEG is invasiveness, which introduces risk of infection, bleeds, strokes, or other complications (<1%) from the surgical procedure, and significant cost (Zaccariotti et al., 1999). Another fundamental disadvantage is that most of the cortex, besides area(s) under the implanted electrodes, remains unexplored. If the seizure onset zone is not covered, iEEG and SEEG techniques might lead to erroneous conclusions. For this reason, these techniques have limitations in investigating the connectivity of cortical networks involved in seizure initiation.

1.3.2 Magnetoencephalography (MEG)

Biomagnetism refers to the magnetic fields produced by living tissues. The first recording of biomagnetic fields was performed on a heart in 1963 (magnetocardiography (MCG)) (Baule and McFee, 1963). The field gained rapid strides as a result of the development of superconducting quantum interference devices (SQUIDs) at the Massachusetts Institute of Technology by James Zimmerman in 1969. Biomagnetism of

the brain is termed as '*Magnetoencephalography*' (MEG) and the first recording was performed in 1971 by David Cohen. Research efforts in the field of biomagnetism have been mostly focused on brain mapping and brain dynamics.

All electric currents produce an electromagnetic field. Communication between neurons is dependent on spiky action potentials and relatively slower excitatory/ inhibitory post-synaptic potentials (E/I PSP). The magnetic field is detected several centimeters away from the source and if produced by a single neuron is difficult to detect due to its extremely weak magnitudes. MEG detection requires that an assembly of neurons fire in synchrony to produce a magnetic field that is strong enough to become detectable by sensors located outside the head. The electromagnetic fields detected by MEG are generated mainly by PSPs. The typical duration of action potentials is extremely short and would require a high-degree of synchronization, which would be difficult to achieve amongst a large enough population of neurons. MEG is able to capture the relatively slower dynamics of PSPs along with the faster activity (~400 Hz) that rides on these slow waves (<100 Hz) (Murakami & Okada, 2006, Cimatti et al., 2007). The magnitude of MEG magnetic fields is in the order of a few tens of femto Teslas.

The SQUID sensors operate at a superconducting temperature. They are cooled using liquid helium to 4.2 K. There are two types of sensors in MEG: magnetometers and gradiometers. A magnetometer consists of a single pickup coil; a gradiometer consists of the pairing of a pickup coil with a compensation coil. The pickup coil detects the strength of the magnetic field that intersects the coil's plane. The compensation coil reduces the noise caused by the interference of sources of nuisance that are assumed to be located

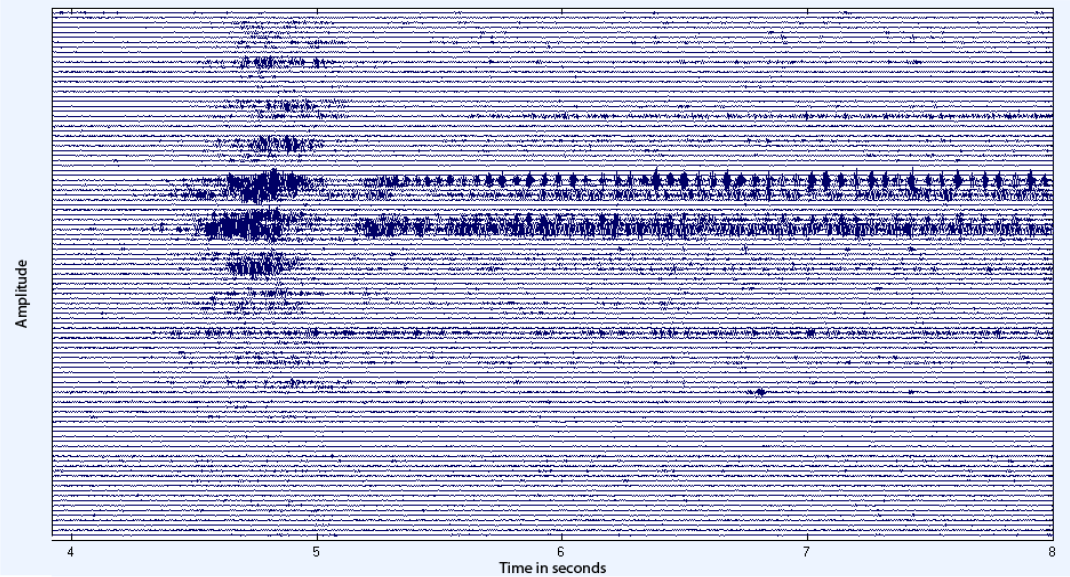

Figure 1.4 Ictal onset. Ictal data captured during pre surgical monitoring. This type of data is generally favored by the clinicians to make decisions for the possible resection of target cortical regions.

farther away. Since the magnetic fields from distant sources produce equivalent current inductions in the pickup and compensation coil, their spatial gradient amounts to null. MEG's time resolution is in the millisecond range, which is a primary advantage over functional MRI (fMRI). Its spatial resolution is about 5 to 10 millimeters under favorable circumstances, which is a major advantage over scalp EEG (Dale and Halgren, 2001).

Since the MEG measures the magnetic field with extremely low amplitude, SNR is one of the key issues. Hence all the MEG recordings are performed in a magnetically shielded room to eliminate the effects of magnetic noise. Dedicated measurements like the electromyography (EMG) and electrocardiography (ECG) are performed to help in removal of muscle artifacts and heartbeats.

1.4 High Frequency Oscillations (HFOs) as an Indicator of Seizure Onset Zone (SOZ)

The SOZ is defined as the area of the cortex where the onset of a partial seizure is generated. The main focus of clinicians has traditionally been on localizing the generators of interictal and ictal events, such as the spike-and-slow-wave complex, for determining the cortical region potentially targeted for resection. A spike is a transient electrophysiological phenomenon that is clearly distinguishable from background activity, with typical durations of 20 to 70 milliseconds. A spike-and-slow-wave complex consists of spike followed by a slow wave. Current data acquisition systems are capable of recording data at high sampling rates (>1000 Hz) at a large number of recording sites (>100). Therefore, analysis of ongoing epileptic data has recently been made possible at unprecedented high-frequency domains of the power spectrum. Recent studies of interictal high-frequency oscillations have revealed what might be new markers of epilepsy, with greater sensitivity than spike-wave events (Zijlmans M et al., 2009, Brázdil et al., 2010). Indeed, it has been proposed that the brain regions sustaining recurrent HFOs may correspond to the SOZ. As a matter of fact, the rate of ictal spikes was found to remain the same after medications while the rate of interictal oscillations was found to decrease post medication consumption (Gotman & Coffler, 1989). AED decreases the likelihood of a seizure and if the rate of interictal spikes were unaffected by AED, then spikes might not be reliable markers of the epilepsy in a given patient. The frequency spectrum covered by HFOs has been proposed to be subdivided into so called ripples (80-200 Hz) and fast ripples (FR) (200-500 Hz), thereby defining potential new biomarkers of the SOZ. However, HFOs have been reported in healthy as well as epileptic subjects, thus

making it difficult to distinguish between normal and pathologic HFOs (pHFOs) so far. It is assumed by several research groups that ripples reflect physiological HFOs, and that FR reflect pHFOs, although the distinction cannot be based on differences in their respective frequency range alone. The location of their generators also plays a major role. Indeed, ripples observed in the dentate gyrus of the hippocampus are considered as pathologic, because such high-frequency oscillatory bursts are generally not observed if the region is healthy. Oscillatory bursts in the range of 200-600 Hz can be observed in the normal neocortex. Ripples have been recorded in healthy controls (Bragin et al., 1999a, 2002b; Staba et al., 2002a, 2004) and are believed to play an important role in synchronizing neuronal activity and might be an essential mechanism to episodic memory (Buzsaki, 2006). Normal high-frequency oscillations are believed to reflect the summation of inhibitory postsynaptic potentials (IPSP), produced by discharges of principal cells (Buzsaki et al., 1992; Ylinen et al., 1995). The degree of synchronization is highly precise to the scale of milliseconds but never reaches a point where an individual neuron becomes unidentifiable from surrounding cells, due to high synchronicity (Engel et al., 2009). The so-called identity of a neuron is analogous to the temporal resolution of data observation, which reflects the ability to accurately predict the amplitude of a signal at a particular instant, though here it reflects in correctly identifying a bursting neuron. During a seizure, the ability to identify a particular neuron is lost since their highly precise synchronization is no longer present, and it gives rise to population spikes.

The first incidence of pHFOs in the range of 250-600 Hz was reported in patients with medial temporal lobe epilepsy (Bragin et al., 1999a). FRs were observed during

interictal periods, as well as during ictal onsets in rodents, thus strengthening the hypothesis of the role of FRs in epileptogenesis (Bragin et al., 1999b, Staba et al., 2002a, Jacobs et al., 2008).

To summarize, HFOs have a frequency in the range of 80 to 500 Hz, a duration in the range of 4 to 6 cycles, and magnitudes of about 3 to 5 standard deviation (STD) from baseline fluctuations at the same location and within the same frequency range (Gardner et al., 2007, Jacobs et al., 2009).

In case of partial epilepsy, the ictal onset is often localized to a single cortical region but the neuronal excitation during the ictal activity may propagate to other regions. pHFOs, if localized and interpreted accurately, might prove as a substantial step forward in the surgical treatment of partial epilepsy, by defining more specific targets for surgery.

1.5 Objectives

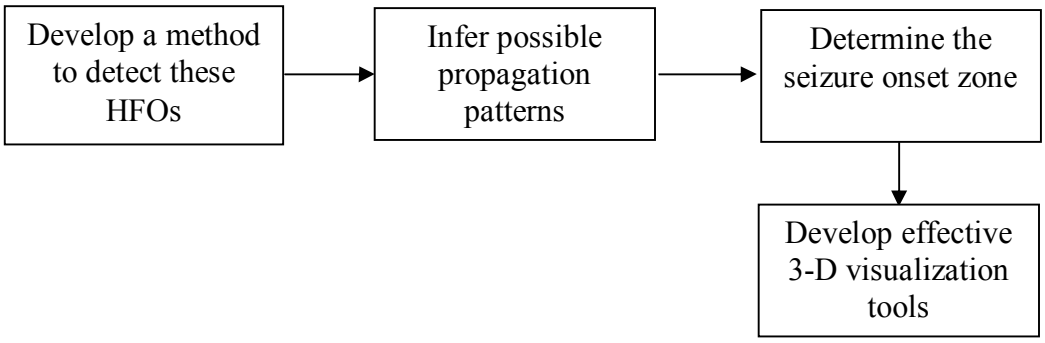

Figure 1.5 Objectives of the project.

We set certain benchmarks that we thought were essential for the completion of the project (Figure 1.5). The first step was to develop a technique that would detect HFOs automatically, since manually marking HFOs is subject to error. In order to test the method, we worked on simulated data before moving on to the physiological data. The next step was to infer possible propagation patterns between different regions exhibiting

strong and sustained HFOs. We then examined different metrics to determine the seizure onset zone (SOZ), and developed a set of effective visualization tools to illustrate the results.

2. METHODS

2.1 Automatic Detection of HFOs Using Wavelet Analysis and the Magnitude of Band-Limited Signals

There can be multiple ways to solve a problem; the important point is not only to solve the problem but also to solve it effectively. We tested two transforms: the wavelet transform and the Hilbert transform to detect HFOs from simulated data. Typically, a signal transformation is applied to the raw data to obtain some information that was not readily interpretable from the raw traces. The performance of the transforms in terms of sensitivity vs. specificity in detecting the HFOs and the computational expenses involved were first determined from synthesized data. The following sections illustrate the methods employed to generate simulated data and automatically determine the HFOs from the simulated and real time series using the techniques we have evaluated.

2.1.1 Generation of Simulated Data

A series of simulated data (simulated baseline + simulated HFO) was generated to evaluate the signal processing techniques we have developed. HFOs were generated at known latencies that were randomly determined and superimposed to simulated background signals, with controlled signal-to- noise ratio (3 to 5 standard deviations from the baseline). We were able to generate a large volume of simulated data, under controlled experimental conditions, which is generally not the case with real, physiological signals, especially under clinical conditions. The algorithm for generating the simulated data was implemented in Matlab (MathWorks Inc., Natick, MA). The

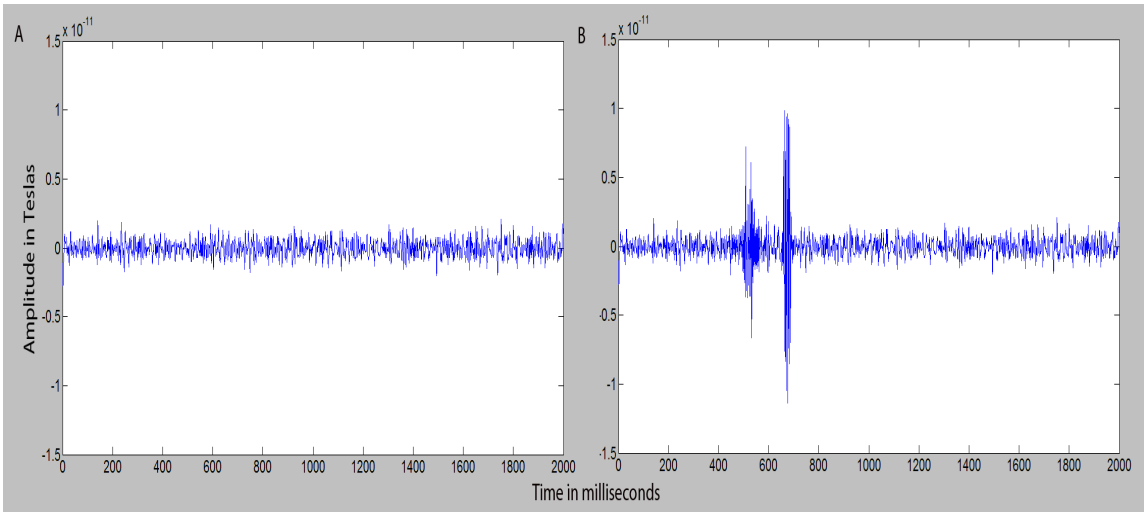

Figure 2.1 Simulated data without and with HFOs. (A) The baseline obtained by averaging over a number of magnetometers (N=50). (B) Simulated data with HFOs added to the baseline signal shown in (A).

simulated data generated using physiological data consisted of background activity with transient oscillatory bursts. A recording of MEG data (102 (number of magnetometers) x 2000 (samples = 2 seconds) was used to generate multiple baseline conditions, onto which artificial HFO bursts could be added. In order to generate a baseline, 50 rows of the MEG data, i.e. signals from a random selection of 50 magnetometers ([50x2000] matrix) were averaged across MEG sensors (resulted in a [1x2000] vector). 300 baseline signals were generated following this procedure. The simulated HFOs were modeled as sine waves that satisfied the properties of physiological HFOs in terms of frequency range (80-300 Hz), duration (4 to 6 cycles) and magnitude (4-6 standard deviations from the background signal). The simulated HFOs were added to the baseline traces at latencies between 350 ms and 1650 ms to avoid contamination from the wavelet edge effects or band-pass filtering (Figure 2.1).

2.1.2 HFO Detection using Wavelet Analysis

The early part of the project consisted of detecting HFOs using wavelet analysis. Wavelet analysis is very useful for non-stationary signals and in situations where it is important to identify features of interest in the signal that are resolved in time and frequency. We first evaluated the bump time-frequency toolbox (ButIF) (http://www.bsp.brain.riken.jp/~fvialatte/bumptoolbox/toolbox_home) that models HFOs as bump features in the time-frequency maps (Vialatte et al., 2007 & Vialatte et al., 2009). This toolbox was available from its authors' website (Riken Institute, Japan). ButIF was implemented in Matlab and Borland C++ builder (2006) (http://www.bsp.brain.riken.jp/~fvialatte/bumptoolbox/toolbox_home) but the whole program can be run from Matlab: The C++ program is executed from the script written in Matlab and the output from the executable file was imported into the Matlab workspace.

Briefly, the method consists of four steps. The first step was to compute the wavelet transform. The second step was to normalize the wavelet transformed map by means of a z-score. The third step consisted of dividing the z-scored map into a set of time frequency windows. The fourth step is a parameterization of these windows by means of half ellipsoid functions to model the HFOs. Once these HFOs were detected, we computed the sensitivity and the specificity. These measures were used to plot the receiver operating characteristic (ROC) curve. These steps are explained in greater details in the following paragraphs.

Complex Morlet wavelets (Figure 2.2) and Mexican hat wavelets are commonly used as mother wavelets for time-frequency signal decomposition. Complex Morlet wavelets have been widely employed for the time frequency analysis of physiological

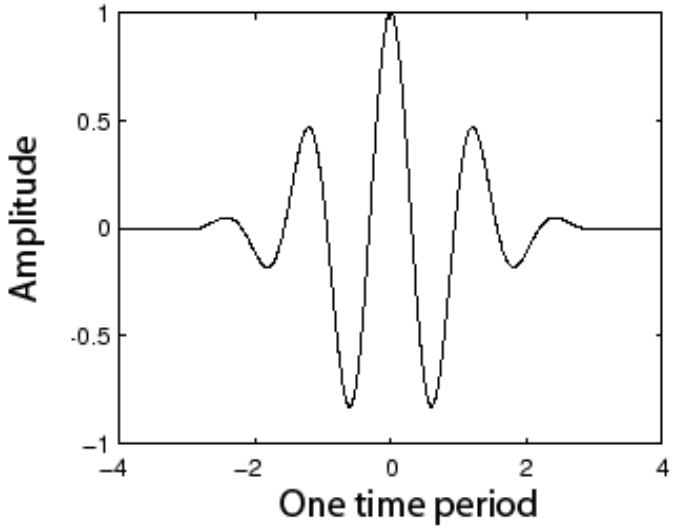

Figure 2.2 Complex Morlet wavelet. The real part of the complex Morlet wavelet data (Vialatte et al., 2008, Düzel et al., 2003, Li et al., 2007). The complex Morlet wavelet is defined as:

$$\varphi\,(t) = \frac{1}{\sqrt{\pi * F_b}}\, e^{2i\pi t F_c}\, e^{\frac{-t^2}{F_b}}, (1)$$

φ: Complex Morlet wavelet;

F_b: Bandwidth parameter (0.5874 Hz);

F_c: Center Frequency (2.0558 Hz);

t: Time

The wavelet function needs to satisfy an admissibility criterion, so that its inverse exists. For the function φ (t) in Eq (1) to satisfy the admissibility criterion, $2\pi F_c t$ should be greater than 5. The wavelet family with $2\pi F_c t=7$ has been shown to be suitable for the investigation of physiological signals (Tallon-Baudry et al., 1996). The complex Morlet wavelet is scaled for computing the wavelet transformation of an original signal X, of length T.

$$C_x(t,s) = \int_T X(\tau) * \psi\left(\frac{\tau - t}{s}\right) d\tau, (2)$$

s: Scaling factor(inversely proportional to central frequency).

C_x: Matrix of wavelet coefficients with dimension: [number of frequency steps x number of time steps].

Ψ: Mother wavelet function

The time frequency map obtained by wavelet transformation was z-scored, with the reference signal being the signal itself (self-referencing). The z-score metric applied at each frequency bin made the events of interest stand out from ongoing fluctuations and standardized the amplitude of the time-frequency signal power. The mean (μ_f) and the standard deviation (σ_f) were calculated for every bin interval (f=80, 85… 300 Hz) and the z-score was calculated based on the equation,

$$Z_f = \frac{C_x(f) - \mu_f}{\sigma_f}, (3)$$

The z-scored map was divided into a set of windows in the time-frequency domain. The width of the windows was fixed to six cycles dependent on the frequency and the height was calculated as the ratio between the width of the window and the time-frequency resolution. The time-frequency resolution was determined by the product of the frequency binning rate (Δf = 5Hz) and the time sampling rate (Δt = 0.001 s). Thus, the value of time-frequency resolution was 0.005. The half ellipsoid function was the parametric function used to model for possible bump features in signal power within the windows defined in the normalized time frequency map. The half ellipsoid function is defined by the equation,

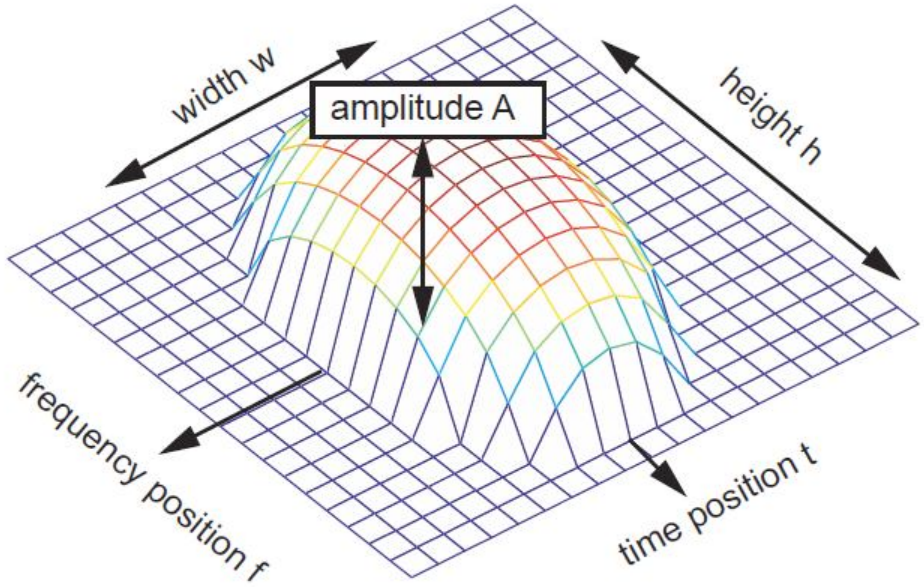

Figure 2.3 Half ellipsoid function. The half ellipsoid functions were defined in the windows that had height h, width w and amplitude A, with positions t and f in the time-frequency domain. Adapted from (Vialatte et al., 2009)**.**

$$\upsilon(A,h,w,f,t,y,x) = 1 - \frac{(y,f)^2}{h^2} + \frac{(x-t)^2}{w^2}, (4)$$

x and y: Time and frequency position of the window on the normalized map;

t and f: Time and frequency position of the bump feature detected;

h and w: Height and weight of the bump;

A: Amplitude of the bump feature.

Figure 2.3 illustrates the shape of the half ellipsoid function and its parameters. Data points lying within the signal power bump were approximated with a non-zero value. All the other points outside the bump and within the time-frequency window of interest were approximated with a null value.

The first two steps, as defined above, were implemented in Matlab (MathWorks Inc. Natick, MA) while the remaining steps were implemented in C++, for optimized

computational performance. The parameters for bump modeling consist of a threshold value, the window dimension and a pruning criterion; they are defined as follows:

The threshold is a numerical z-score value that helps remove events related to normal background activity. All values below the user set threshold value are not considered further in the analysis. The threshold value was varied from 0 to 15 in steps of approximately 0.3. In order to model the bumps accurately at different frequencies, the dimension of the time-frequency window of interest needs to be adaptive. In order to capture events at higher frequencies the window should be short and vice-versa. The windows have a large time width that decreases with increase in frequency to account for the intrinsic time resolution of the wavelet decomposition. Symmetrically, and for the same reason, window height was designed to increase with frequency. The time width of the window was fixed to six cycles (the assumed typical duration of HFOs) to avoid the detection of sporadic and spurious high-frequency bursts. Indeed, if the time width of a window was set too long, multiple and successive oscillatory events would be modeled as a single event. Similarly, too short a time window would artificially split a single event into multiple events. A pruning parameter was used to set the maximum number of bumps to be modeled. The parameter was set to 100, a relatively high value (a two second data segment was assumed to accommodate a maximum of 100 events having duration of six cycles and frequency of 300 Hz). The detected bumps were sorted in descending order of power. If the maximum number of detectable bumps was set to a very small value, events of interest would go undetected; a very high number of detectable bumps would lead to detection of bumps with less power in case the user set threshold was small in magnitude, as shown in the Results section.

2.1.3 HFO Detection Using the Hilbert Transform

The primary reason for switching to another technique in the course of this project was to design an alternative signal processing technique that would be more computationally efficient than the comprehensive wavelet decomposition used with ButIf. Further, the ButIF implementation consisted of recurrent transfers of data between Matlab and an executable C++, which increased the time of computation. The reason for selecting Hilbert transform approach (extraction of instantaneous magnitude of the band-limited signal) was its ability to preserve the original temporal resolution of the data and to restrict the analysis within the HFO frequency band of interest. The simulated data with HFOs was generated in the same way as those used for testing the performance of the wavelet decomposition approach. The data time series were first band-pass filtered into five sub-bands (80-124, 125-169, 170-214, 215-259 and 260-300 Hz) before the Hilbert transform was applied. The FIR filter was applied in the frequency domain with an order of (number of samples-1).

The Hilbert transform is a widely used approach to compute the analytic version of signal time series. An analytic signal is a complex signal obtained by taking a signal and adding in quadrature its Hilbert transform. If we have a real signal x_r and we compute the Hilbert transform, x_i, of the signal, the analytic signal x is a complex function represented by $x=x_r + i*x_i$, where x_i is the 90^0 phase-shifted version of x_r. The Hilbert transform x_i of x_r is defined for all t by,

$$x(i) = \frac{1}{\pi}\, PV \int_{-\infty}^{\infty} \frac{x(\tau)}{t-\tau}\, d\tau, (5)$$

when the integral exists, where PV is the Cauchy principal value.

The Hilbert transform does not exist, due to a pole, at $t = \tau$. The Cauchy principal value in front of the integral means that integral on either side of τ (which may exist) is computed and thus, it expands the class of functions for which the Eq (5) exists. The magnitude of the complex analytic signal provides the envelope of x_r (Dujundgi, 1958). This envelope is temporally smooth if the signal is band-limited in a narrow range and it is expected to be spiky if the signal is filtered within a wider range of frequencies (Figure 2.4). The z-score of the signal envelope was computed and a threshold was applied to detect events of interest, i.e. occurrences of transient high-magnitude variations in the signal envelope, in the HFO frequency range. Only events of duration between 4 and 6 cycles were retained.

2.1.4 Performance Evaluation

In order to determine the respective performances of the suggested signal transformations, we considered two factors: sensitivity and specificity. Sensitivity measures the proportion of true positives in the detection of events of interest; specificity measures the proportion of true negatives. In the context of HFO detection, sensitivity measured the proportion of actual HFOs correctly detected and specificity measured the proportion of correctly detecting the absence of HFOs.

$$Sensitivity = \frac{True\ Positives}{True\ Positives + False\ Negatives} \qquad (0 \leq \text{Sensitivity} \leq 1)$$

$$Specificity = \frac{True\ Negatives}{True\ Negatives + False\ Positives} \qquad (0 \leq \text{Specificity} \leq 1)$$

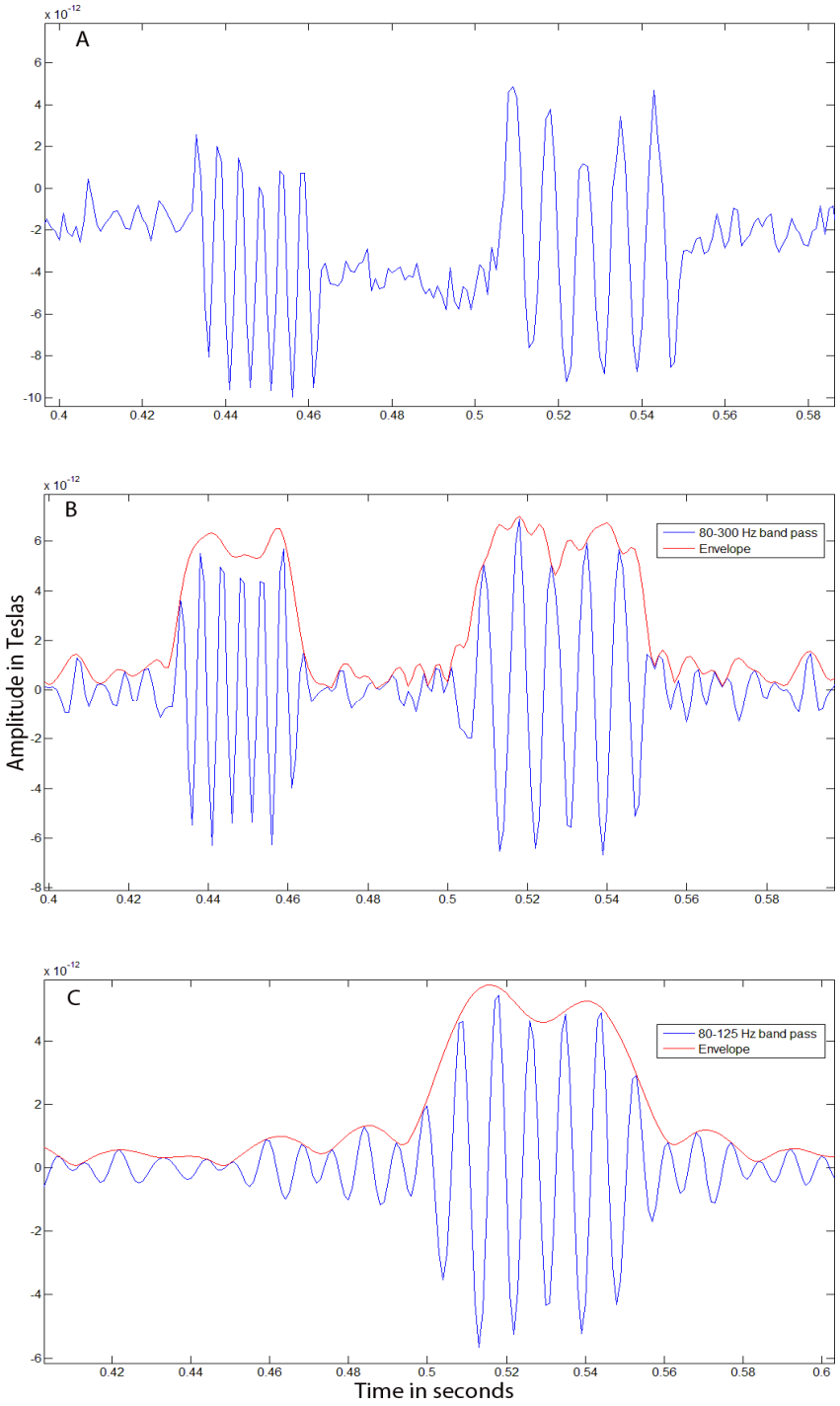

Figure 2.4 Effect of narrow band-pass filtering. A) Original simulated signal. B) Raw signal band-pass filtered (blue) in the range of 80-300 Hz. C) Original signal, band pass filtered in the range of 80-125 Hz. The envelope (red) obtained using the Hilbert transform was smoother in the case of a narrow band-passed signal in panel C as compared to the wider band-passed signal shown in panel B.

The sensitivity and specificity performance metrics are usually inversely related: lower detection thresholds increase sensitivity and decrease specificity, and vice-versa. The receiver operating characteristic (ROC) curve illustrates this trade-off and helps determine a possible optimum value for the detection threshold. It is a classical approach in the design of techniques for signal detection from noise. A ROC curve is a plot of sensitivity on the y-axis, and (1-specificity) on the x-axis. As the area under the curve approaches 1, the better is the performance of the detection technique. The sensitivity and specificity were determined for different thresholds and the ROC curve was plotted.

Since the data was simulated, exact time information of the occurrences of the HFOs were known prior to the transformation. The threshold was varied from 0 to 15 in steps of 0.3, to obtain a smoothly varying ROC curve. In order to determine the sensitivity and the specificity for a particular threshold, we determined the true positives, false positives, true negatives and false negatives. These values were determined by dividing each of the two-second simulated signal segments into sliding windows of length 50 milliseconds with no overlap. Each window was checked for the presence or absence of HFOs. If there was an actual and detected HFO, the true positive score was incremented. If there was an actual HFO and it was not detected by the algorithm, the false negative score was incremented. If there was no actual HFO but the algorithm gave a false detection, the false positive score was incremented. If the window had no actual HFO and the algorithm also did not pick up any event, the true negative score was incremented. Determining true positive, false positive and false negative was straightforward since the event times when the HFOs were present or absent were known. True negative determination was not straight forward and its value depended on the

window size. The choice of the size of time window was arbitrary but it was selected so that the window was neither too small nor too large. The window size was chosen with respect to the expected duration of HFO events. A HFO with a frequency of 80 Hz and duration of four cycles would last for 50 ms and thus we selected this value as a conservative estimate for the screening time window. Determination of the sensitivity and the specificity at a particular threshold was performed and this procedure was repeated for every tested threshold. The resulting ROC curve was plotted, which not only provided a visual impression of the performance of the detector, but also helped in determining the optimum threshold for the best tradeoff in sensitivity and specificity. The optimal threshold was defined as the point of intersection between a line joining the points (1, 0) & (0, 1) and intersecting the ROC curve.

2.2 Subjects

We retrospectively analyzed data from three patients with medically refractory partial epilepsy who underwent 2-stage epilepsy surgery at the Froedtert and Medical College of Wisconsin's Adult Comprehensive Epilepsy Program. The patients were selected based on the presence of robust, well-defined epileptic HFOs in their intracranial EEG recordings prior to undergoing resective surgery. All patients had undergone prior MEG recordings as part of their final pre-surgical evaluation. Relevant clinical variables for these patients are shown in Table 2.1. Patients 1 and 2 were seizure free at 12 months post surgery. Patient 3 experienced a single cluster of auras and complex partial seizures over a 5-day period, 4 months after surgery in the context of antiepileptic medication reduction, but did not experience further events at 6 months post-operative follow-up.

2.3 Development of Matlab Scripts Compatible with Brainstorm

Brainstorm (http://neuroimage.usc.edu/Brainstorm) was one of the neuroimaging software that was extensively used in the course of the present project for the analysis of the MEG data and visualization of both the MEG and of the ECOG data. A serial processing pipeline was developed in Matlab using scripts that integrated Brainstorm and our Matlab specific developments. Once a minimum number of inputs were provided, data processing was carried out automatically unless an input from the user was paramount, e.g. when indicating the anatomical fiducials for the registration of MEG and MRI geometry. The processing pipeline consisted of a set of serial steps; the following subsections illustrate the purpose of each step.

ID	MRI lesion	iEEG electrodes	iEEG HFOs	MEG spikes	Ictal iEEG	Resection zone
1	Left MTS, bilateral PVH	L subdural grid + strips	Left TP	Left TP	Independent onsets left AT & TP	Left ATL + hippocampus + TP neocortex
2	None	L subdural grid + strips	Left AT neocortex	None	Left AT neocortex	Left AT neocortex
3	Old R mid temporal tumor resection age 2 yrs	R subdural grid + strips	Right TPO	Right TPO	No ictal iEEG data captured	Right TPO neocortex & mesial temporal structures

Table 2.1 Clinical variables. Abbreviations used above are as follows: MTS—mesial temporal sclerosis, PVH—periventricular heterotopias, TP—temporo-parietal, AT—anterior temporal, TPO—temporo-parieto-occipital.

2.3.1 Obtaining Cortical Surfaces and the Electrode Positions

Platinum-iridium alloy electrode discs (4mm diameter) were arranged in a grid (8x8/6x6), partial grids (5x2) and strips (4x1) (Ad-Tech Medical, Racine, WI). Electrodes were placed in the subdural space through craniotomy and burr hole craniotomy. IEEG recording was performed at a sampling rate of 1000 Hz. Patient specific 3D cortical surfaces were obtained (Dale, et al. 1999, Fischl, et al. 1999, Fischl, et al. 2002) by processing the MRI data (LaViolette, et al. 2010) using FreeSurfer (http://surfer.nmr.mgh.harvard.edu/). CT data was co-registered using a linear affine transformation to post-implant MRI data using FLIRT (FMRIB software library http://www.fmrib.ox.ac.uk/fsl) and resampled to the original MRI resolution. CT data was thresholded to isolate iEEG electrode locations. The centroid location of the voxel cluster corresponding to each electrode was found and defined in the same geometrical referential as the MRI data. Thus, we obtained the electrode coordinates that were used extensively as described in later subsections.

2.3.2 Generating the Surface Envelopes for Cortex, Inner Skull, Outer Skull and Scalp

The second step was to generate the cortex envelope, inner skull, outer skull and the scalp using the *'mne_watershed_bem'* function of the MNE neuroimaging software (http://www.nmr.mgh.harvard.edu). These surfaces helped in the visualization of the head with respect to the sensors and cortex, and in the correct alignment of the cortex with respect to the head.

2.3.3 Creating Protocol, Condition and Subject Entries in Brainstorm Database

Brainstorm's database is structured in a very orderly manner. At the top of the tree is the Protocol (name of the study). The protocol name of this study was *'freesurfer_subjects'*. Once the protocol was created, we needed to name the condition under which the recording was performed. Since the data we were analyzing was spontaneous data, the condition was named as *'Spontaneous'*. After creating a condition, we needed to create a new subject database entry. Subjects and conditions both came under the protocol, i.e. once a protocol was selected; we were able to list subjects based on a condition or alternatively, list conditions based on the subject.

2.3.4 Importing MRI and Marking the Fiducials

The next step was to import the subject's MRI from the FreeSurfer subject directory into Brainstorm. The FreeSurfer subject directory contained information about the structural data of the subject. Once the subject's MRI was imported, fiducials namely the nasion, left and right pre-auricular points were marked (Figure 2.6 and 2.7). We obtained the coordinates of these fiducials in the coordinate system used in MEG. Hence we were able to obtain the transformation matrix from the coordinate system used in the MRI (FreeSurfer coordinate system) to the MEG coordinate system (coordinate system defined from the subject's head surface).

2.3.5 Generating Grid and Strip Surface Objects

In case of iEEG, we had each grid and strips placed on the subject's cortex. We derived a method to visualize the data obtained from the grid and strip electrodes using grid and strip surface objects in Brainstorm's 3D visualization tools. A series of transformations were applied to the electrode coordinates to move them into the FreeSurfer coordinate system. The coordinates of the electrodes were originally in voxel values and were expressed in millimeters. They were first converted into meters and then the voxel coordinates were transformed into FreeSurfer coordinates using the following transformations:

$$(x, y, z) = 0.128 - (x, y, z)$$

$$(x, y, z) = (x, -z, y)$$

The MRI freesurfer values has the center in approximately [128,128,128] voxel. Using the FreeSurfer coordinates and the script *'mne_write_surf',* we generated the grid and strip surfaces for each patient in the FreeSurfer space. This ensured that the grids and cortical surface were in the same referential (FreeSurfer) as the other surfaces. The grid and strip surfaces were generated using different methods in the course of this project. The number of points representing electrodes on the grid and strips was too small (N=64 to 106) to produce a smooth distribution of data for visualization purposes. Hence, we used an interpolation method to increase the number of points for each electrode object detected on the grid and strips. The method for interpolating the grid was straightforward: the electrode coordinates were passed to the function *'nsi_sensorpos2triC'* (developed at the lab, by Dr. Rey Ramirez) and the extra points on the grid were computed.

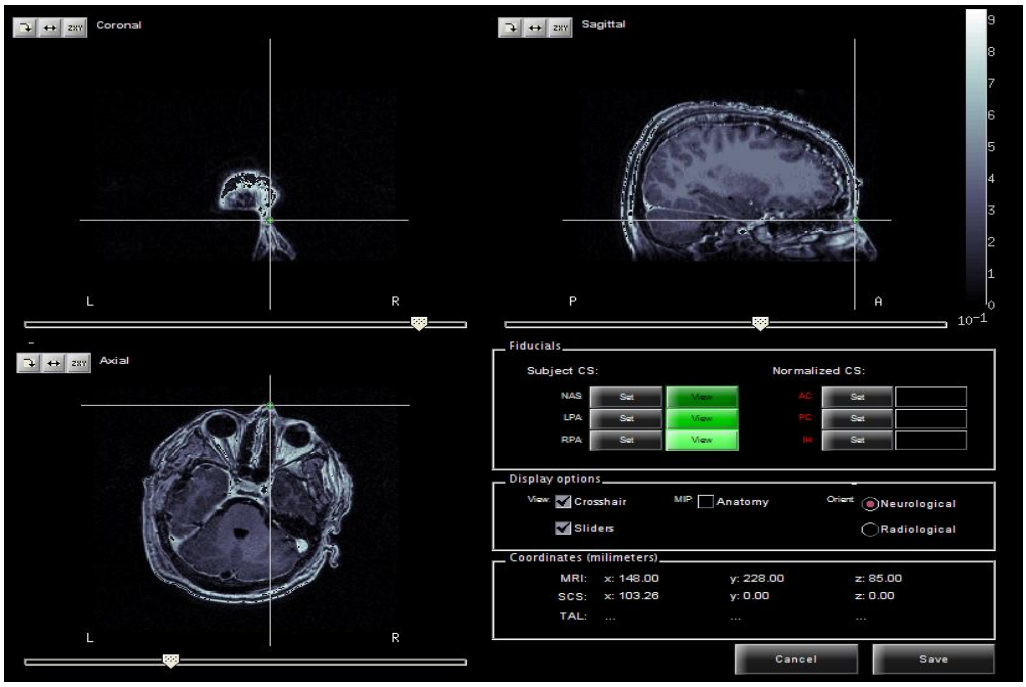

Figure 2.6 .Marking of nasion using the MRI. The figure shows the nasion in the axial, coronal and sagittal views of the subject's MRI. The nasion is the point of intersection of the lines in all the views

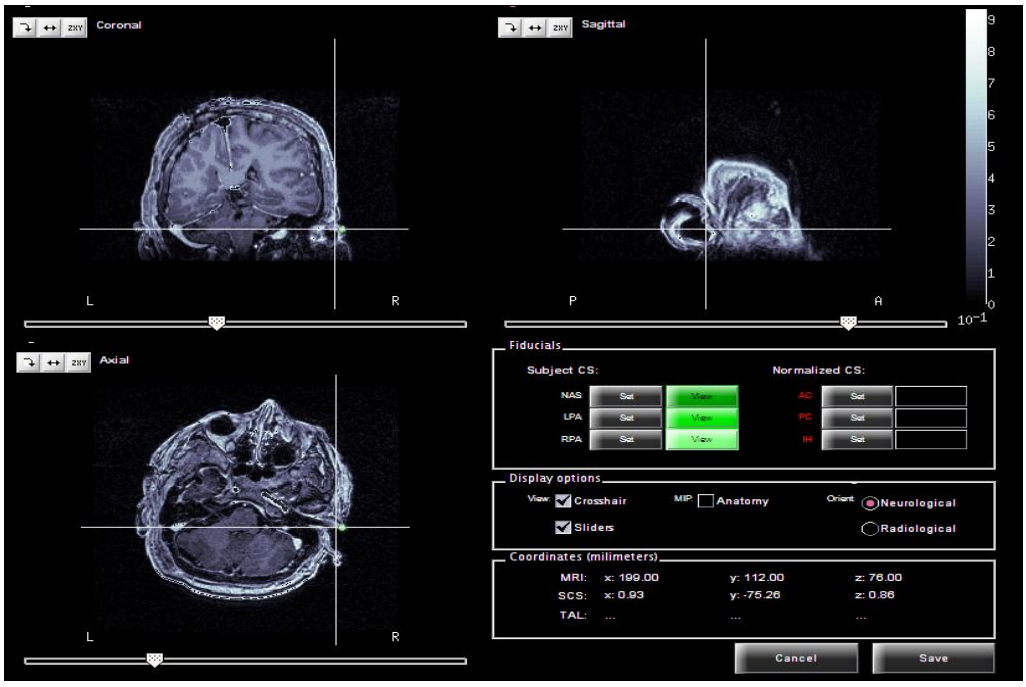

Figure 2.7. Marking of right pre-auricular point using the MRI. The figure shows the right pre-auricular point in the axial, coronal and sagittal view of subject's MRI.

The function computes a face matrix from a set of points in space (electrodes or vertices) by using multidimensional scaling and delaunay triangulation. The face matrix and the vertex matrix are the two matrices needed by Matlab to plot a surface.

The interpolation of electrodes on the strips was more complicated because the electrodes were positioned on almost a straight line and thus the script was unable to perform interpolation. We, basically, needed to artificially increase the width of the electrode strip so that reliable interpolation could be performed. Thus, we had to extrapolate first in order to later perform an interpolation. In order to extrapolate, we needed to find points that were located 2 mm (arbitrary) on either side of the strip electrode. They were determined by applying a method based on singular value decomposition (SVD), as explained below.

In 3-D, perpendicular unit vectors define a perpframe (orthonormal vectors). Any matrix can be decomposed as a product of three matrices: the hanger, the stretcher and the aligner, i.e. a matrix A can be written as a product of (Hanger)*(Stretcher)*(Aligner). (http://www.uwlax.edu/faculty/will/svd/index.html). This decomposition is determined bySVD. In 3-D, the hanger matrix rotates the x-y-z axis to align with the perpframe. The stretcher matrix stretches (or quashes, or flips) a point or a surface in the x, y or z direction. The aligner matrix rotates the perpframe to align along the x-y-z axis. In order to compute coordinates 2mm on either side of the strip electrodes, we multiplied the coordinates with 2mm*[the hanger matrix], to obtain the coordinates of points 2mm on either side. The *'nsi_sensorpos2triC'* could then be applied, which yielded a set of interpolated vertices for the strips. Once we obtained the interpolated points, we used '*mne_write_surf*' to generate the strip surfaces in the FreeSurfer space.

2.3.6 Importing the MEG Data

The MEG data was imported into Brainstorm database using its function *'import_data'*. The data was divided into segments of 2 seconds, which made it easier for the software to load, visualize the sensor data and compute the source model.

2.3.7 Computing the Head Model

Head model computation was required to explain how the neural currents in the cortex could generate the MEG sensor data. Head modeling is also known as *forward modeling*. Forward modeling consists of computing the magnetic field recorded at the sensors from a given distribution of source density; inverse modeling is computing the source time series that produced the magnetic fields previously recorded.

The head model generates a lead-field matrix, which models the linear correspondence between the source amplitudes and the MEG data. In Brainstorm, it was

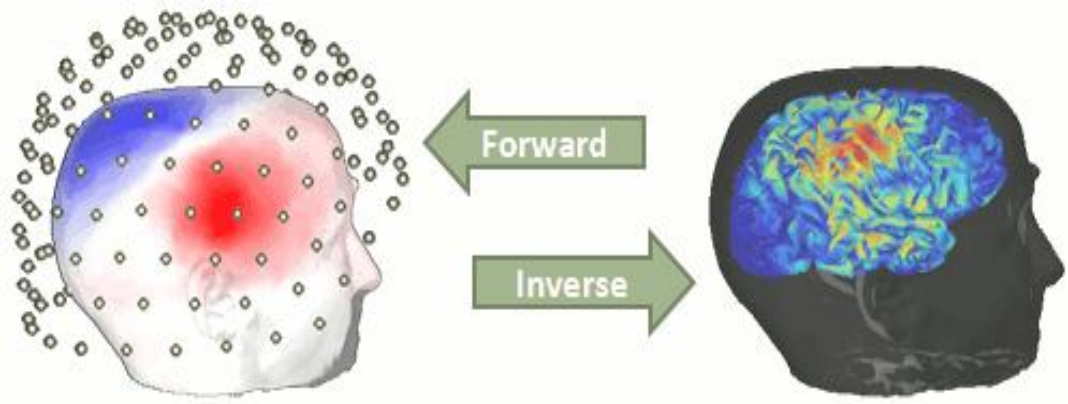

Figure 2.8. Forward and inverse modeling. In order to transition from the sensor space (left) to the source space (right) we need to solve the inverse problem. Adapted from www.neuroimage.usc.edu

considered that the magnetic field recorded by the sensors was produced by set of elementary current dipoles distributed on the cortical surface. The dipoles were located at each of the vertices of the cortical surface tessellated by FreeSurfer. We limited the number of elementary dipoles or sources to 10,000 per cerebral hemisphere; hence a total of 20,000. The lead-field head model was a matrix of size; Number of sensors*Number of sources i.e. [306 x 20000] matrix. Different methods are available in Brainstorm to compute the head model: the single sphere and overlapping spheres. In the single sphere method, a single sphere is fitted to approximate the shape of the head. Overlapping spheres modeling consists in estimating different spheres of the head for every sensor (Baillet et al., 2001). In other words, it estimated a sphere that best fits the shape of the head. It has been acknowledged that spherical models perform quite well in the MEG, because head in the vicinity of each sensor. The spherical head models are an approximation to the realistic head models, since a normal head is not spherical. MEG is less sensitive to head geometry than EEG (Leahy et al., 1998). To keep the model simple, we used the single sphere model to complete the head model in all 3 patients. The computation of the head model was performed by the function *'Hil_head_model',* which called basic functions from the Brainstorm library.

2.3.8 Computing the Noise Covariance Matrix

In order to compute the inverse operator (imaging kernel) for the source reconstruction process, we needed to estimate the noise covariance matrix from the MEG data. The signal to noise ratio (SNR) remains as one of the key issues in MEG due to extremely low amplitude signal of interest when compared to strength of other

electromagnetic sources (heart beats, eye blinks etc). In the context of studying task-related evoked responses, the background brain activity might be considered as a source of nuisance (although this is certainly an oversimplifying assumption). In the case of source modeling of spontaneous recordings, the environmental and instrumental noise within the magnetically shielded room is a source of nuisance. The empirical estimation of the noise covariance statistics is a necessary step to improve the accuracy of source modeling (Sekihara et al., 1994, Sekihara et al., 1996). The function *'bst_noisecov'* was used to compute the noise covariance matrix. A default empty room recording of 2 minutes was used to compute the noise covariance matrix (NC),

$$NC = \frac{LL'}{Number\ of\ time\ points};$$

where,

L contains the measurements from the empty room [306*Number of time points]. Whitening and regularization procedures are employed to refine the noise variance matrix. Whitening helps to remove any correlation between the sensors.

2.3.9 Computing the Source Signals

Computing the source signals consists of solving an inverse problem. It involves computing an inverse operator or in other words, an imaging kernel. The imaging kernel is a matrix of size [Number of sources x Number of sensors] i.e. [20,000 x 306]. Parametric source localization and source imaging are two types of techniques for computing the source signals in MEG. Parametric techniques represent the sources as a set of few equivalent current dipoles of unknown locations and moments, which can be

estimated from the data using non-linear optimization techniques. Source imaging approaches assume that the cortical pyramidal neurons are the main source of MEG signals and are oriented perpendicular to the cortical surface. Every vertex of the cortical tessellation was assumed to be a dipole source with its orientation constrained to the local normal of the surface. Thus, only the amplitude needs to be estimated from the MEG data, using a linear estimator for instance. Since we needed to estimate source signals from 20,000 vertices and data was obtained from 306 sensors only, the inverse problem was severely underdetermined. In that respect, under-determinacy yields an ill-posed problem, wherein multiple source distributions would produce the same output as observed on the sensors. In order to better constrain the estimation problem, we applied regularization methods to apply additional constraints and estimate the locations of sources on the cortical surface.

Brainstorm employs an imaging technique for solving the MEG inverse problem. Since the dipoles were restricted to the cortex, the FreeSurfer cortical surface needed to be of very high resolution and should capture the sulci and gyri accurately because if those were missed, essentially the dipole sources would be missed and hence source signals at those areas would be undetected. The dipoles were constrained to fixed positions and the inverse operator consisted of a minimum-norm estimator of the source distribution (Baillet et al., 2001; Tikhonov and Arsenin, 1977; Demoment, 1989).

2.4 Localization of the SOZ from Interictal and Ictal iEEG Data

The main aim of localizing the HFOs was to detect the areas that were involved in the seizure onset, i.e. the cortical regions that were active at the beginning of seizure

events. Therefore, we needed to rank the channels/sources based on their temporal occurrence (rank with a small value correspond to earlier involvement in HFO bursts). These bursts visually showed propagation from one cortical region to others in the case of partial epilepsy. The method based on the Hilbert transform (see above) was used to analyze both the interictal and ictal data. Hence, after the HFOs from each channel were detected, they were ranked based on their temporal occurrence. The channels with the smaller ranks determined the channels/sources of interest. In the case of iEEG, the cortical regions under the lower ranked electrode sites were the areas of interest, whereas in MEG, the sources with lower ranks determined the cortical regions of interest. The detailed method to determine the SOZ is illustrated in the following paragraphs.

2.4.1 Interictal and Ictal Data

The patients were kept under observation and their medication was reduced so that the patient was prone to seizure. The spontaneous recording was carried out over several days until a sufficient number of seizures were captured, so that a strong evidence for resecting a particular region could be collected. The period between seizures, i.e. interictal period, when there were HFO bursts on a consistent basis were selected for analysis. Table 2.2 illustrates the period of bursts selected for analyzing interictal and ictal data. The data was acquired at a sampling frequency of 1000 Hz and the sources analyzed were restricted to cortical regions under the electrodes.

Subject	1	2	3
Interictal iEEG	3.1 mins	7.2 mins	4.8 mins
Interictal MEG	5.01 mins	5.08 mins	2.15 mins
Ictal iEEG	1 sec	1 sec	-
Number of seizures analyzed	3	3	-
Number of electrodes	106	76	73
Number of sources	3367	2019	2944

Table 2.2 Volume of interictal and ictal data analyzed. Amount of time analyzed for the interictal and ictal data of all subjects and number of electrodes/sources used for recording/analyzing the data.

2.4.2 Analysis of Interictal iEEG Data

The aim of our analysis was to localize the seizure onset zone or in simple terms, identify the leading region generating the HFO bursts and to determine the propagation pattern of HFOs, for more specific resection during epileptic surgery. The steps required in order to analyze the iEEG data is illustrated in figure 2.9. The Hilbert transform was applied to the interictal data, which had been band-pass filtered in different frequency bands, in order to compute the envelope of the signal. The z-score of the signal envelope for each electrode site was computed and the mean and standard deviations for all the channels were saved onto the hard disk for future computational purposes. A higher threshold (Th=5) than the optimum threshold (Opt_th=4.19), obtained from simulations

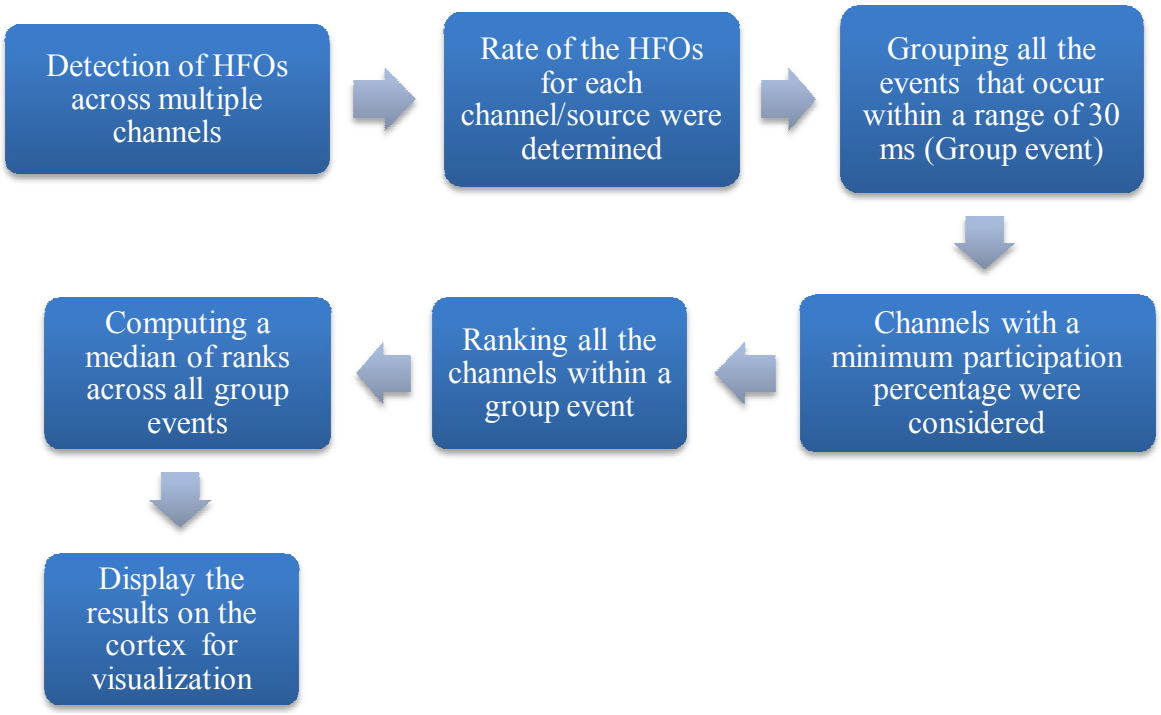

Figure. 2.9 Steps for analyzing interictal iEEG and MEG data. The flow chart illustrates the steps used to compute the rank and rate metrics for both interictal iEEG and MEG data. Detailed explanation of the flowcharts is provided in the sections below.

(see above) was applied to z-scored signals since a higher threshold increased specificity, which was necessary for our task. The number of events detected for all the channels were determined, which would indicate the cortical regions that produced a larger number of HFO bursts. We generated a map indicating the rate of HFO firing at each site. Once all the HFO events were detected for every channel, they were grouped based on their temporal occurrence and were named as group events (Figure 2.10). In order to be grouped together, two events detected on two different channels needed to occur within a 30 millisecond range or else they were not grouped. This value was set arbitrarily based on visual observations of our data by an expert epileptologist. For a group event to be considered for temporal analysis, there should be a minimum of five channels involved in a group event. A parameter called '*Min_grp*' was set to 5 in our scripts. If fewer channels

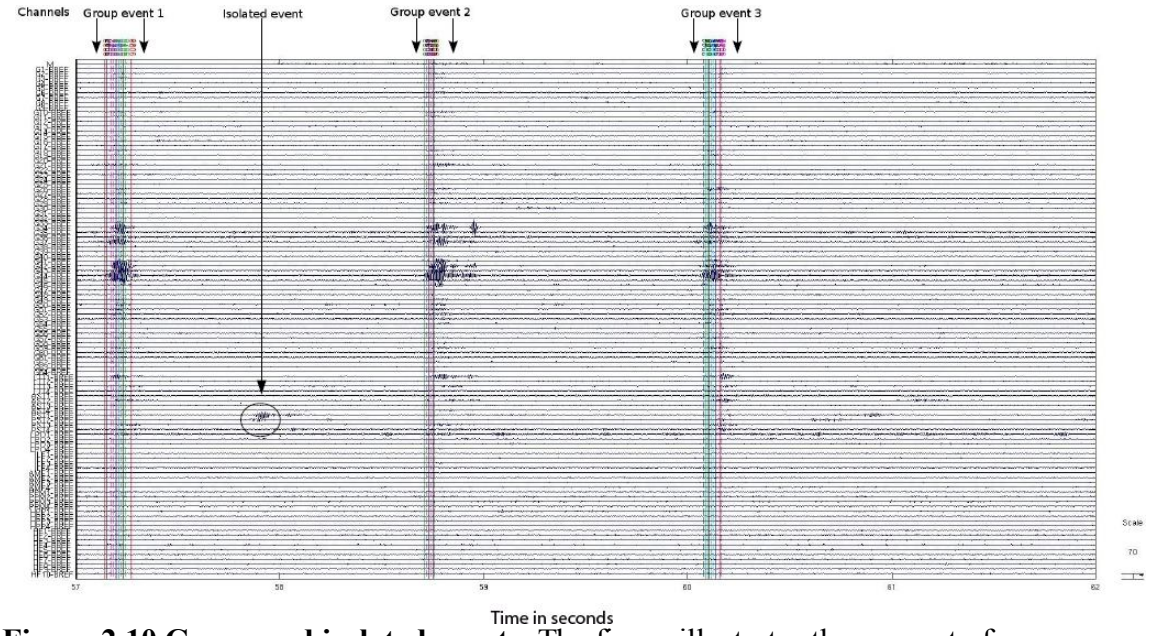

Figure 2.10 Group and isolated events. The figure illustrates the concept of a group event. A group event consists of the detection of HFO bursts across multiple channels, and that are temporally close to one another. There were three group events detected by our algorithm in this example. The agreement with visual observation was considered as good. Isolated events were not considered in the analysis. The vertical lines between the two arrows of a particular group are the event markers illustrating the times these HFOs were detected at different electrode sites.

were involved, we assumed it did not reflect propagation on a larger scale. This setting was also suggested by the expert neurologist. The channels needed to be involved in a certain percentage of group events (20%), a parameter termed '*Per_rem'*. For instance, if there were 20 group events detected across the entire recording, for a channel to be considered it needed to be present in at least 4 of those 20 group events. The reason to introduce this parameter was that, if an electrode was involved in just one event and by chance was ranked to be one, its overall rank would remain one and would reflect an inaccurate result. To summarize, a particular group event should have a minimum of five events from different electrodes that occurred within 30 ms of one another (i.e. maximum duration between first and fifth event from different channels would be 150 ms) and an electrode site should participate in at least 20% of the group events to be retained for

further analysis. The electrode sites were then ranked for every group event based on their temporal occurrence. The electrodes that were not active during the oscillatory bursts were assigned a rank greater than the maximum rank assigned to an electrode that participated in a burst. The median statistics of the ranks for every electrode site was computed.

To further clarify the approach, let us consider an imaginary example where there were 50 electrodes, and about 20 group events were detected across a five minute recording. For the first group event, let us assume that about 10 electrodes sites carried sustained HFOs and that the others remained silent. We ranked the 10 electrodes based on the temporal occurrence of their respective HFO events and all the silent electrodes were assigned an arbitrary late rank with a value of 11 (10+1) for subsequent visualization purposes. This process was repeated for all group events (N=20). Hence, every electrode was assigned 20 rank values, one for every group event, and the median of these 20 values for every electrode was computed.

For Subject 2, during the placement of the cortical electrode grid, the wire to one of the 2-D strips was disconnected and the data could be only recorded from 64 electrodes out of total 76 electrodes. Hence, we performed a supplementary interpolation step to account for the missing electrodes: For each missing electrode, the three nearest electrodes out of the 64 electrodes were determined by their Euclidean distance, and the average of the time series of those three electrodes was computed to determine the time series of the missing electrode.

We needed to visually represent the results to better identify the cortical regions involved (i.e. the areas beneath the electrodes) and the propagation patterns of the HFOs.

In the previous subsection, we described how we generated the FreeSurfer grid and strip surfaces and imported them into the Brainstorm database. The grid and strip surfaces were interpolated to determined additional vertices for better visualization. The number of vertices on the interpolated grid and strips were about four times as many as the number of electrodes used to record the iEEG data. The interpolated vertices were assigned the ranks of the nearest electrode sites; hence a very simple form of nearest neighbor interpolation of the ranks. Although this introduced regions whose activity could not be verified due to absence of electrodes at those regions, this simple form of data interpolation was intended to facilitate visualization of the data. The resulting visualization of the data is featured (Figure 2.11). One rank or HFO rate value was assigned to each vertex on the grid and strip surfaces: the results were saved as a .mat file that could be imported into the Brainstorm database and visualized using Brainstorm visualization tools.

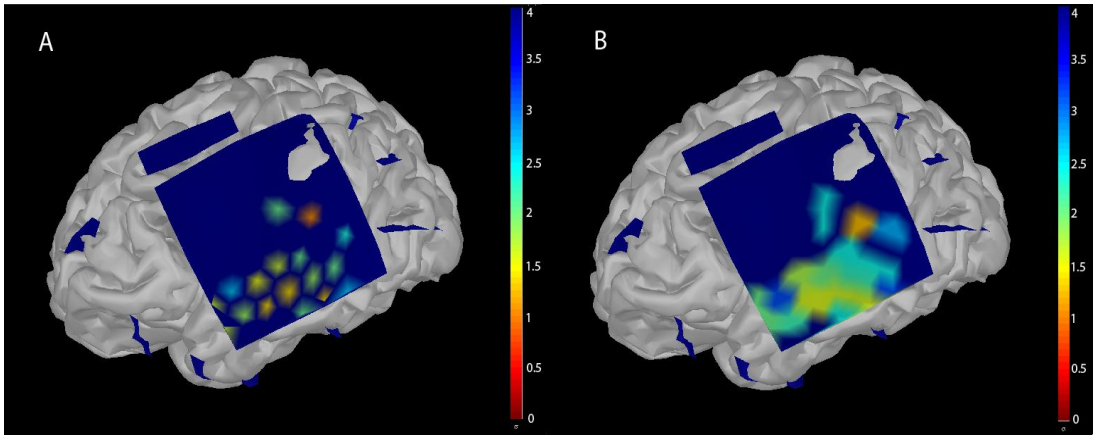

Figure 2.11 Data interpolation. Data interpolation was performed to enhance visualization. A) Data without interpolation. B) Data with interpolation. The figure with interpolation was not only visually more appealing but also helped better understand the distribution and propagation patterns of HFOs.

2.4.3 Analysis of Ictal Data

Although the overall methodology remained the same, the ictal data was analyzed in a slightly different way than interictal data. Ictal episodes involved more regions in one group event at the ictal onset and lasted for a short period of time. We were interested in identifying the cortical regions (SOZ) that pulled other regions to a seizure and this information is present at the beginning of a seizure. Five seconds around the ictal onset was selected and two seconds in the beginning and the end of the signal were removed to avoid edge effects introduced by band-pass filtering. Thus, only one second at the ictal onset was considered. Once the seizure gained full strength, the data became too complex to identify a clear propagation pattern and hence the entire seizure was not used in the analysis. Interictal data or spontaneous recording was considered as a baseline to the ictal onset. The means and the STDs of different frequency bands for all the channels computed from the interictal data in the previous section were used to compute the z-score for the ictal data. Since the ictal data to be analyzed was very short in duration (1 s), computing the z-score by self -referencing (i.e. using ictal data to compute means and STD) would have affected the z-score in a negative manner. For instance, the channels that were oscillating would have a higher STD and thus a lower z-score, which would be inaccurate. To summarize, five seconds around the seizure were considered, out of which 2 seconds at the beginning and end were eliminated to avoid edge effects; so the signal analyzed was just one second about the electrographic onset of the ictal event. The rest of the process followed in the same way as interictal data. Three seizures each, from the first two subjects, were analyzed and their spatial and temporal characterization using the techniques described above were compared with the

localization of interictal events. The data from the third subject was analyzed based on interictal data only. No seizure had been captured during the pre-surgical monitoring of this patient, and the surgery plan was based on propagation patterns observed during interictal recordings (and the semiology of seizures).

2.5 Localization of the SOZ from Interictal MEG Data

The number of vertices extracted from the FreeSurfer surface was down-sampled from original 2,00,000 to 20,000 due to the tradeoff between spatial accuracy and computational load of MEG source imaging. A greater number of vertices would necessitate more computer memory, whereas fewer vertices would generate source images of poor spatial resolution. The clinical evaluation of the SOZ location was obtained from the expert reading of iEEG recordings of each patient. IEEG, as opposed to MEG, is not an exploratory procedure per se, primarily due to its invasiveness. The amount of skull bone surgically removed by craniotomy is restricted to a minimum and

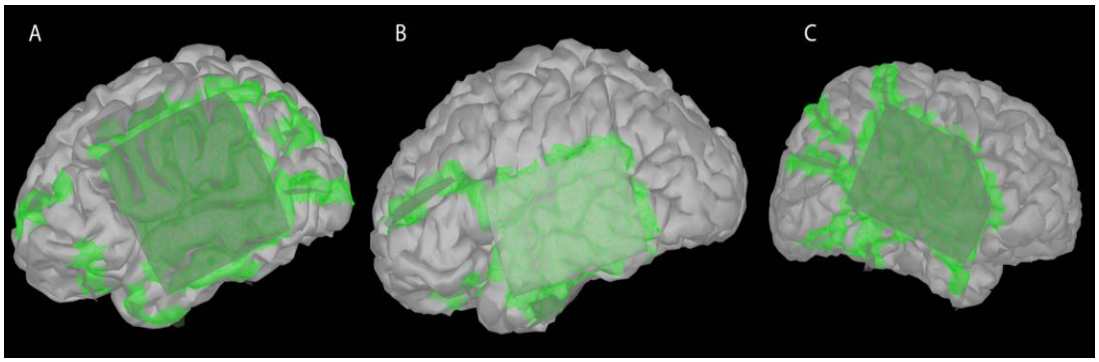

Figure 2.12 Area of the cortex selected for evaluation. Panel A, B and C represent the cortical surfaces for subjects 1, 2 and 3 respectively. For comparison of iEEG and MEG the analysis of MEG sources was restricted to the area of the cortex covered by iEEG electrode sites. The darker grey areas represent the grid and the strips. The areas colored as green were the areas of the cortex where the MEG sources were compared to iEEG traces, in terms of HFO metrics.

the cortical regions explored with iEEG are confined to the areas covered by the strips and the grids. MEG imaging techniques were used to produce estimates of cortical currents covering the entire surface of the cortex. In order to compare the results obtained by MEG and iEEG, we restricted the analysis of the MEG data to the areas of the cortex located under iEEG electrode sites. This was accomplished by means of an algorithm we have developed. The closest cortical vertices (Euclidean distance) to each of the vertex corresponding to the electrode sites were determined. For instance, from 421 vertices corresponding to the original electrode sites, we found 421 seed vertices on the cortex based on minimum Euclidean distance. All the cortical vertices that were less than 4 mm away from each of the seed vertices were determined. Some of the sources that were missed by our method, due to its location in the fissures, were marked using scout functions in Brainstorm. The scout in Brainstorm's terminology defines an area of interest over the cortical surface defined by interactive 3D visualization. Figure 2.12 illustrates the areas of cortex to be analyzed that were determined using this method.

2.5.1 MEG Data

The spontaneous data was acquired for each of the three subjects with a sampling frequency of 2,000 Hz (Table 2.2). This permitted analysis at higher frequencies (<600 Hz). The data was acquired by means of 102 magnetometers and 204 gradiometers. An empty room recording of two minutes was used to compute the noise covariance matrix.

2.5.2 Analysis of MEG data

As mentioned above, the analysis of MEG source time series was restricted to areas under iEEG electrode sites.. We obtained a matrix by selecting the rows of the imaging kernel corresponding to the sources and multiplied the matrix by the sensor data to obtain the source data at the sites of interest. It was the source data to be analyzed since it reflected the physiological signal captured by the sensors. The HFOs were detected using the technique described above. The number of HFO events per source location was determined, as per the methods described previously. The detected HFOs were grouped based on their temporal occurrence by the algorithm as discussed in the previous sections, and the average ranking of events occurring at each source location was determined. The minimum number of sources to be classified as a group event were raised to 100 since there were more than 2000 sources to be analyzed for every subject (Table 2.2).

A *'spiking index'* metric was computed for all sources under consideration. The spiking index is defined as the maximum value of source amplitude over the mean value of the entire source time series (5.01 mins for subject # 1).

$$SI = \frac{X_{window\_max}}{X_{entire\_mean}}$$

where,

SI: represents the spiking index of a source;

X_{window_max}: represents the maximum value in a particular frequency band within a pre-selected window determined by the algorithm over the time series X of the source;

X_{entire_mean}: represents the mean over the entire recording in the same frequency band.

As a brief example, let us assume that 1000 MEG sources were covered by iEEG electrode sites and 20 group events were detected over the course of five minutes of spontaneous recording. Let us now consider the first group event. Let us define that the first event detected in this group was at time x and that the last event in this group was detected at time y. The time interval from two seconds before time x and two seconds after time y was included in the analysis, i.e. the time range of the data that was used to compute the spiking index was from (x-2) seconds to (y+2) seconds. About one second from the beginning and the end was removed to avoid the edge effects. The source data was band-pass filtered in the five sub-bands of interest and their envelope using the Hilbert transform was computed for all the pre-selected sources. The mean amplitude

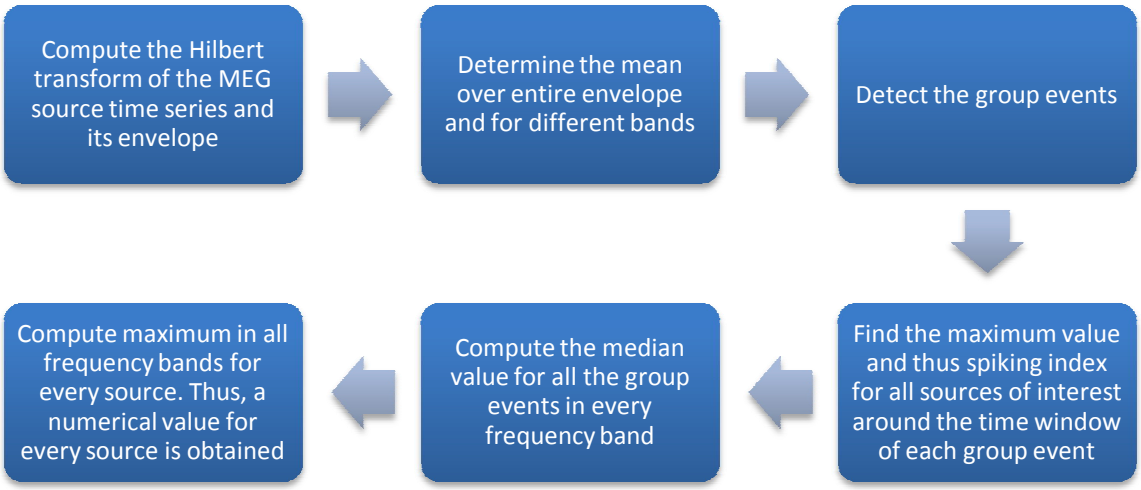

Figure 2.13 Steps to compute the spiking index. The flow chart illustrates the steps used to compute the spiking indices.

value for each source over the entire recording for the five sub-bands was calculated. The maxima in the time window (x-1) seconds and (y+1) seconds were computed for all the signal envelopes in the five sub-bands. The spiking index could now be calculated since we had the maxima and the mean value over the entire source time series at different frequency bands. This process was repeated for all group events. Thus, we obtained a matrix of size [1000*5*20] (number of sources*number of sub-bands*number of group events). The median value for every source across the 20 group events for every sub-band was calculated and the median measure matrix was reduced to [1000*5]. The maximum value for all the sources in every sub-band was calculated to eliminate the frequency dimension and the measure matrix was reduced to a vector of length 1000. These values were then saved as a .mat file to utilize Brainstorm visualization tools.

3. Results

3.1 Accuracy of HFO Detection

Our first aim was to detect the HFOs using an algorithm that would eventually help us in the determination of the seizure onset zone. HFOs detected by the algorithm had to be tested against actual HFOs in order to calculate its sensitivity and specificity and therefore we generated sine waves that satisfied the properties of HFOs. The artificially generated HFOs were then added to the simulated baselines that were generated using the physiological data. We tested two methods for detection, the ButIf toolbox that implemented wavelet transforms and a method based on the Hilbert transform of data signals for detecting the HFOs.

The general flow employed for detecting HFOs using the ButIf toolbox and the Hilbert transform is explained in the previous Methods section. Figures 3.1 and 3.2 illustrate the HFO detection for one such simulated signal. The same set of simulated data was used for both methods to enable a fair comparison. Also, for a particular method, the same set of simulated data was used to calculate the sensitivity and specificity for all thresholds varying from 0 to 15. Table 3.1 provides a comprehensive illustration of the sensitivity and specificity values at different thresholds for both the methods and these values were used to plot the ROC curves. From Table 3.1, the values of specificity at a particular threshold for Hilbert transform approach was higher than the wavelet technique. The ROC curves for both methods are shown in Figure 3.3 and provide a clear picture of the performances of the two techniques. A trapezoidal numerical integration method was used to determine the area under the ROC curves. The area under the curve

obtained using the ButIf was 0.8 while the area under the curve using Hilbert was 0.93, indicating a better performance in terms of sensitivity/specificity tradeoff for the latter. The optimal threshold for the ROC curve obtained using the Hilbert transform was 4.2.

	ButIf toolbox		Hilbert transform	
Threshold	Sensitivity	Specificity	Sensitivity	Specificity
0	0.98	0.09	0.99	0.01
0.31	0.98	0.09	0.99	0.02
0.61	0.98	0.09	0.98	0.07
0.92	0.98	0.09	0.97	0.14
1.22	0.98	0.09	0.96	0.25
1.54	0.98	0.09	0.95	0.38
1.84	0.98	0.09	0.94	0.53
2.14	0.98	0.09	0.94	0.68
2.45	0.96	0.14	0.93	0.79
2.76	0.95	0.23	0.93	0.86
3.06	0.94	0.34	0.93	0.91
3.37	0.94	0.45	0.92	0.94
3.67	0.93	0.55	0.91	0.95
3.98	0.93	0.64	0.90	0.96
4.29	0.92	0.71	0.88	0.96
4.59	0.91	0.77	0.86	0.97
4.90	0.90	0.81	0.84	0.98
5.20	0.89	0.84	0.81	0.98
5.51	0.88	0.86	0.77	0.98
5.82	0.85	0.88	0.74	0.98
6.12	0.83	0.90	0.70	0.99
6.43	0.78	0.91	0.66	0.99
6.73	0.73	0.93	0.63	0.99
7.04	0.68	0.94	0.58	0.99
7.35	0.66	0.95	0.53	0.99
7.65	0.56	0.96	0.49	0.995
7.96	0.49	0.97	0.44	0.997
8.27	0.42	0.97	0.39	0.998
8.57	0.36	0.98	0.34	0.999
8.88	0.30	0.98	0.30	0.999
9.18	0.25	0.99	0.27	0.999
9.49	0.19	0.99	0.24	1

	ButIf toolbox		Hilbert transform	
Threshold	Sensitivity	Specificity	Sensitivity	Specificity
9.80	0.15	0.99	0.22	1
10.10	0.12	0.99	0.20	1
10.41	0.09	0.995	0.17	1
10.71	0.07	0.996	0.15	1
11.02	0.05	0.997	0.13	1
11.33	0.03	0.999	0.12	1
11.63	0.02	0.999	0.09	1
11.94	0.01	0.999	0.06	1
12.25	0.004	1	0.03	1
12.55	0.004	1	0.01	1
12.86	0.003	1	0	1
13.16	0.003	1	0	1
13.47	0.001	1	0	1
13.78	0.001	1	0	1
14.08	0	1	0	1
14.39	0	1	0	1
14.69	0	1	0	1
15	0	1	0	1

Table 3.1 Sensitivity and specificity values for both HFO detection methods computed at different thresholds. The Hilbert approach had much greater specificity values and comparable sensitivity values to the ButIf toolbox.

3.2 Localization of SOZ Using iEEG and MEG

We analyzed the spontaneous interictal iEEG and MEG recording for three subjects and ictal iEEG recording from two of these subjects. IEEG data was acquired at a sampling rate of 1000 Hz and thus we restricted our analysis up to 300 Hz to comply with the Nyquist criterion. The MEG data was acquired at a sampling rate of 2000 Hz but for comparison purposes with iEEG the analysis was restricted up to 300 Hz. IEEG recording was performed until a few seizures were captured. The ictal data obtained was

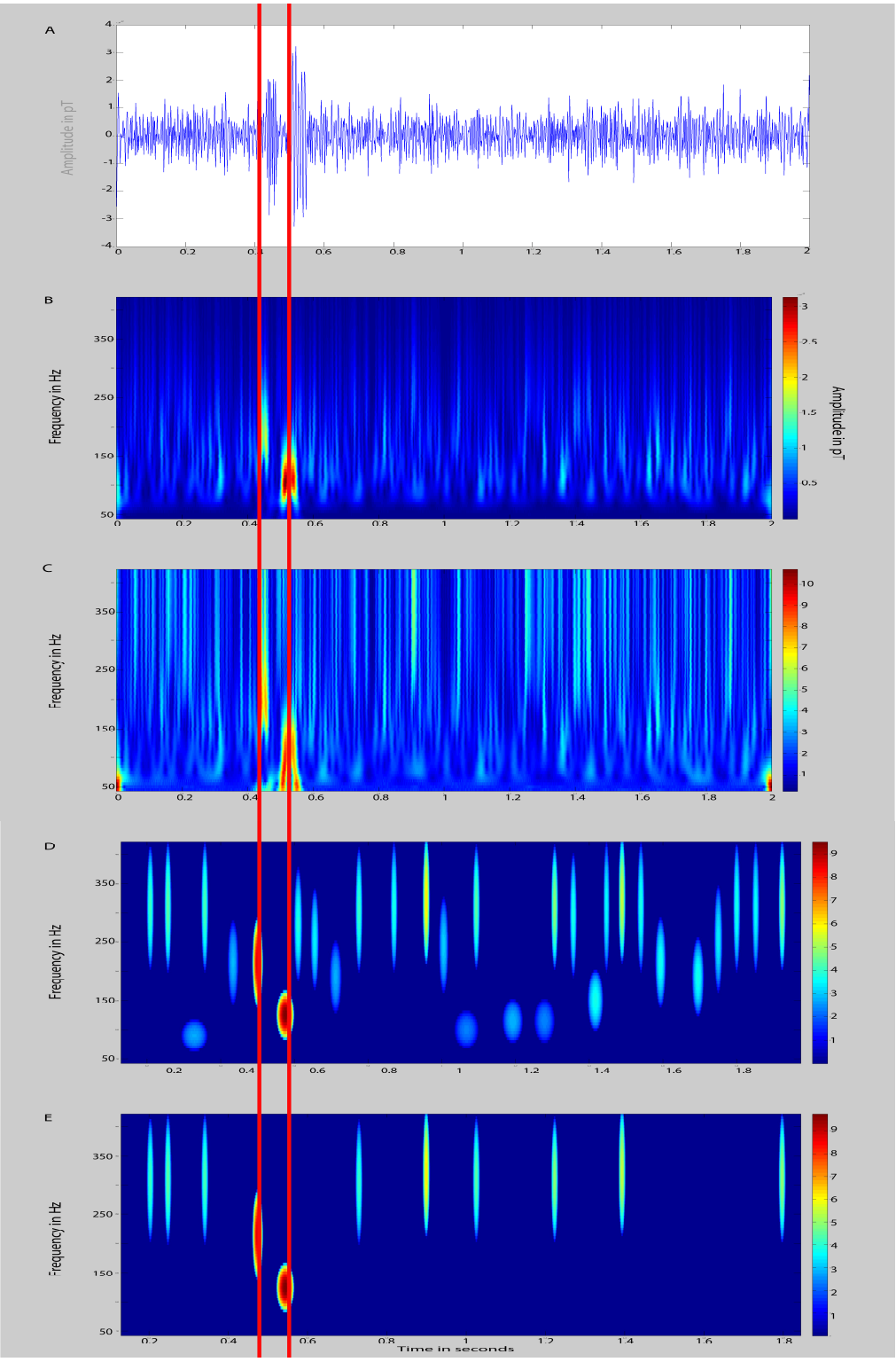

Figure 3.1 HFO detection using the ButIf toolbox. (A) Simulated signal that was band-pass filtered in the 80-300 Hz range. (B) Wavelet transformation of the simulated signal. (C) Normalized time-frequency map computed by means of z-score. The edges of the map were discarded to avoid false detections due to the wavelet border effects. (D) The

bumps were detected with low threshold (Th=0.3) applied using the half-ellipsoid model in ButIf (see Methods section). (E) Bumps with lower energies were discarded by applying a threshold of 4. The two vertical red lines indicate the actual HFOs.

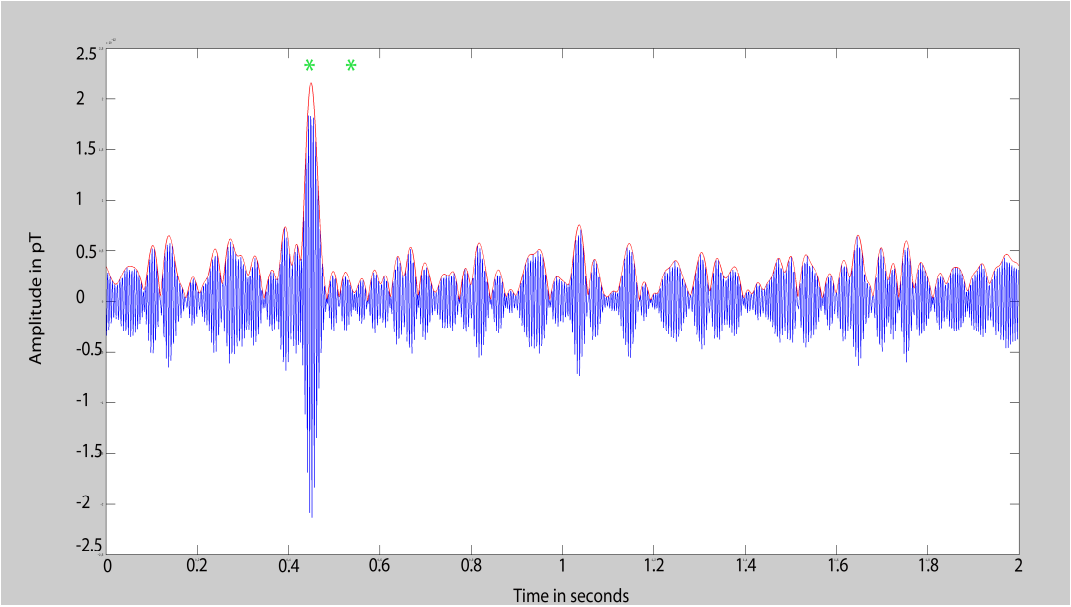

Figure 3.2 HFO detection using Hilbert transform. The signal (in blue) was the same simulated signal as used in figure 3.1. The signal was band-pass filtered within the 169-213 Hz frequency range (one of the HFO sub-bands of interest). The other event with a frequency in the range of 80-125 Hz was eliminated by filtering (red asterisk). The red curve represents the envelope of the band-passed signal. The green asterisk indicates the HFO event detected by the method with a threshold of value 4.

used to make clinical decisions regarding resections prior to surgery. The portion of interictal recording, showing HFO bursts across channels on a consistent basis, was selected for analysis. The MEG recording analyzed was spontaneous data. The HFO rate map provided the rate of bursts at each electrode/sources site during the recording. The HFOs events were then grouped and ranked based on their temporal occurrence. Ranking the channels/sources provided valuable information regarding the channel/source leading the propagation of these oscillatory bursts, which eventually, provided the information regarding a possible location for the SOZ. The clinical decisions are made based

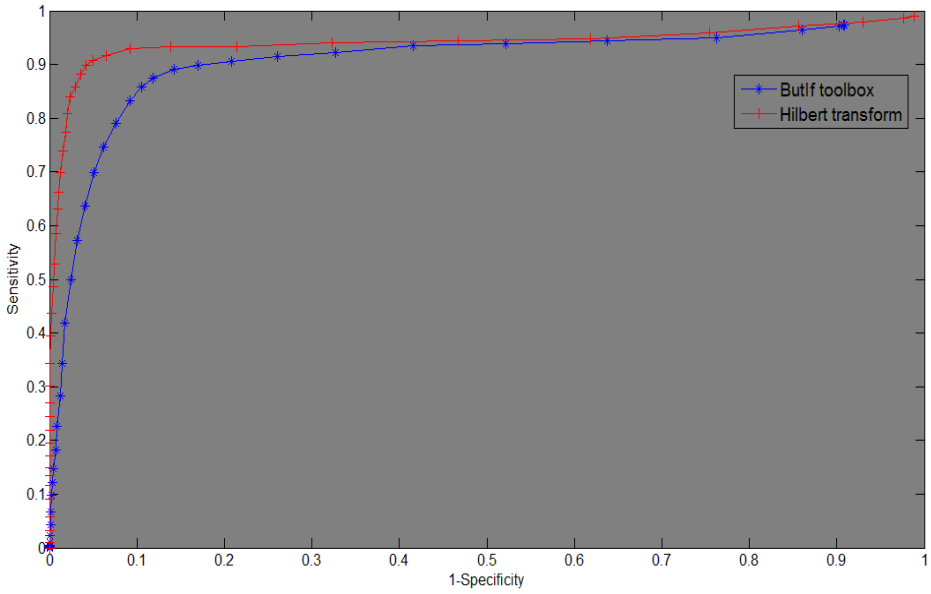

Figure 3.3 ROC curves. The ROC curve (red curve) obtained from the Hilbert transform had an area under the curve closer to one than the ButIf toolbox (blue curve).

essentially on ictal data and hence comparing the results of the ictal data and interictal data was expected to indicate the differences and similarities.

The brain regions with HFOs were marked by the neurologist and were compared with the outcome of the algorithm (Figure 3.4). The regions are marked on the grids and stips itself. Figure 3.5 indicates the SOZ localization for subject 1. The HFO rate map obtained from iEEG data localized the regions around the post central gyrus and the superior temporal gyrus that produced the maximum number of HFOs. The MEG map strongly localized the maximum HFO rates to the post central gyrus, posterior temporal region and the lateral parietal occipital region. The HFO ranking method using iEEG localized the SOZ to the post central gyrus and superior temporal gyrus. The HFO ranking using the MEG data was difficult to interpret due to the large number of contributing source sites that were analyzed within a very small region of coverage.

Figure 3.4 HFO map of subjects as marked by a neurologist. Columns show the lateral and the ventral view respectively, of the cortex for the subjects. The dark red colored areas indicate the cortical regions where the HFOs bursts were observed by inspection of the data by an epileptologist.

The regions with lower ranks were located about the pre and post central gyrus. Ictal event # 1 localized to the post central gyrus and the posterior temporal gyrus. Ictal event # 2 localized to the post central gyrus and the posterior temporal gyrus. The ictal events and interictal recording showed good concordance with respect to localization of the SOZ. The spiking index map of the sources for subject 1 localized to the post central gyrus, posterior temporal region and the lateral parietal occipital region (Figure 3.6). The cortical regions localized to very similar regions as localized using the rate map or the rank map.

Figure 3.7 shows the localization of the SOZ of subject 2. The HFO rate map obtained using iEEG interictal data localized the maximum HFO rates to the anterior temporal gyrus and posterior middle temporal gyrus. The MEG data localized the maximum HFO rates to the anterior region of inferior temporal gyrus and the left temporal tip. The ranking of the HFOs using iEEG data localized the SOZ to the anterior temporal gyrus. The ranking of the HFOs using the MEG data also localized to anterior temporal gyrus and middle temporal gyrus. Ictal events # 1 and # 2 both localized the SOZ to the anterior region of the inferior temporal gyrus.

Figure 3.8 represents the spiking indices of subject 2 for all the sources in non-normalized and normalized form. The values of spiking indices without normalization were very similar for all the sources and therefore we normalized it to reveal the regions with a higher spiking index. We normalized the spiking indices based on the maximum and minimum value to adjust the colorbar range from 0-1. The enhanced regions localized to the anterior temporal gyrus and the middle temporal gyrus as localized by the rate map and regions with low ranks.

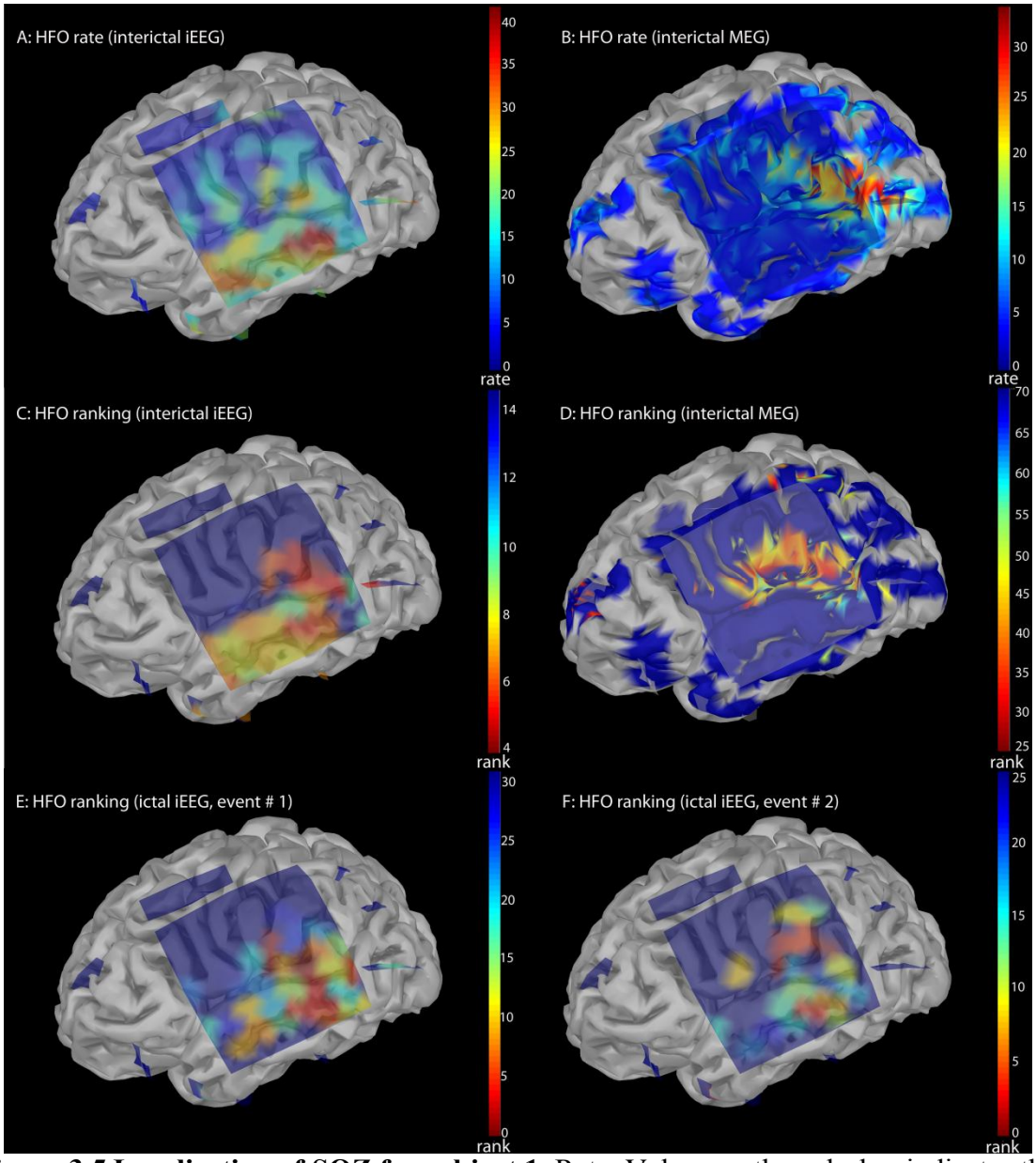

Figure 3.5 Localization of SOZ for subject 1. Rate: Values on the colorbar indicates the rate of HFO bursts of the sources/electrodes. Rank: Temporal precedence over other channels. Channels with low ranks burst before the channels with higher ranks on average. **(**A) Rate of the HFO bursts captured by the electrodes during interictal iEEG recording. (B) Rate of HFO bursts detected from each of sources analyzed using the MEG interictal data. (C) Rank of the channels obtained using the same interictal iEEG recording as used to A. Channels with low ranks are classified as SOZ. (D) Rank of the sources obtained using the interictal MEG data. (E) Rank of the channels using the first ictal iEEG recording. (F) Rank of the channels using the second ictal iEEG recording.

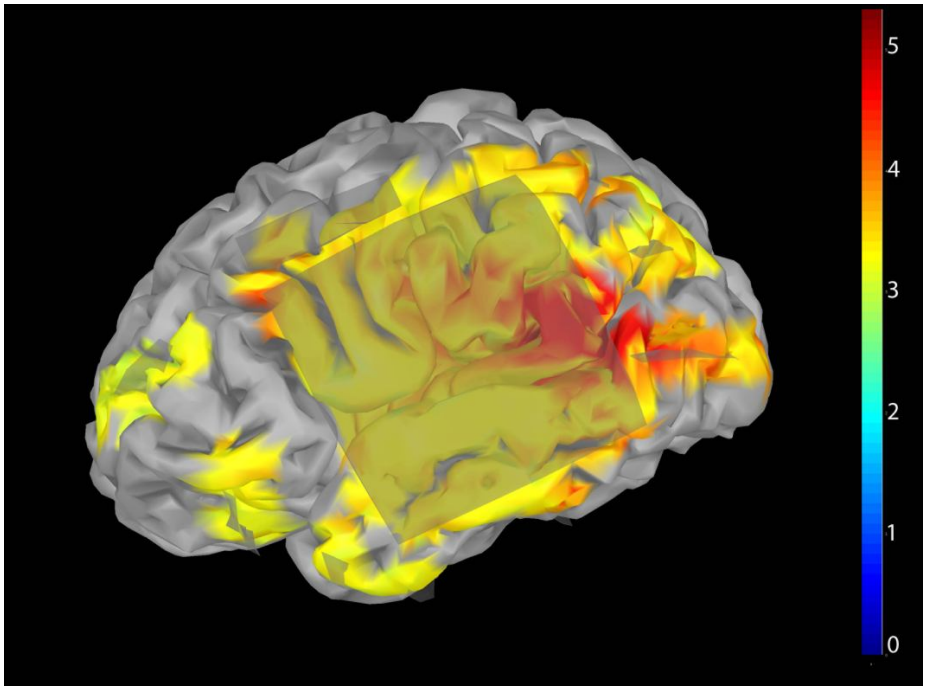

Figure 3.6 Map of MEG spiking indices for subject 1. The spiking index value for all the sources. The regions with maximum values localized to the same regions as the rate or the rank map in Figure 3.5.

Figure 3.9 and 3.10 illustrates the spiking indices and localization of SOZ for subject 3. The HFO rate map obtained using iEEG interictal recording localized the highest HFO rates to the sub-temporal occipital region and the mid parietal occipital region. HFO rate map obtained using the MEG recording localized to the sub-temporal occipital (STO) and sub-temporal region anterior (STA) to the STO. The ranking of the HFO bursts using iEEG localized the SOZ to the STO. The ranking of the HFO bursts obtained by the MEG recording localized the SOZ to the STO, STA and posterior inferior occipital regions. The sources with higher spiking indices also localized to the STO region (Figure 3.9).

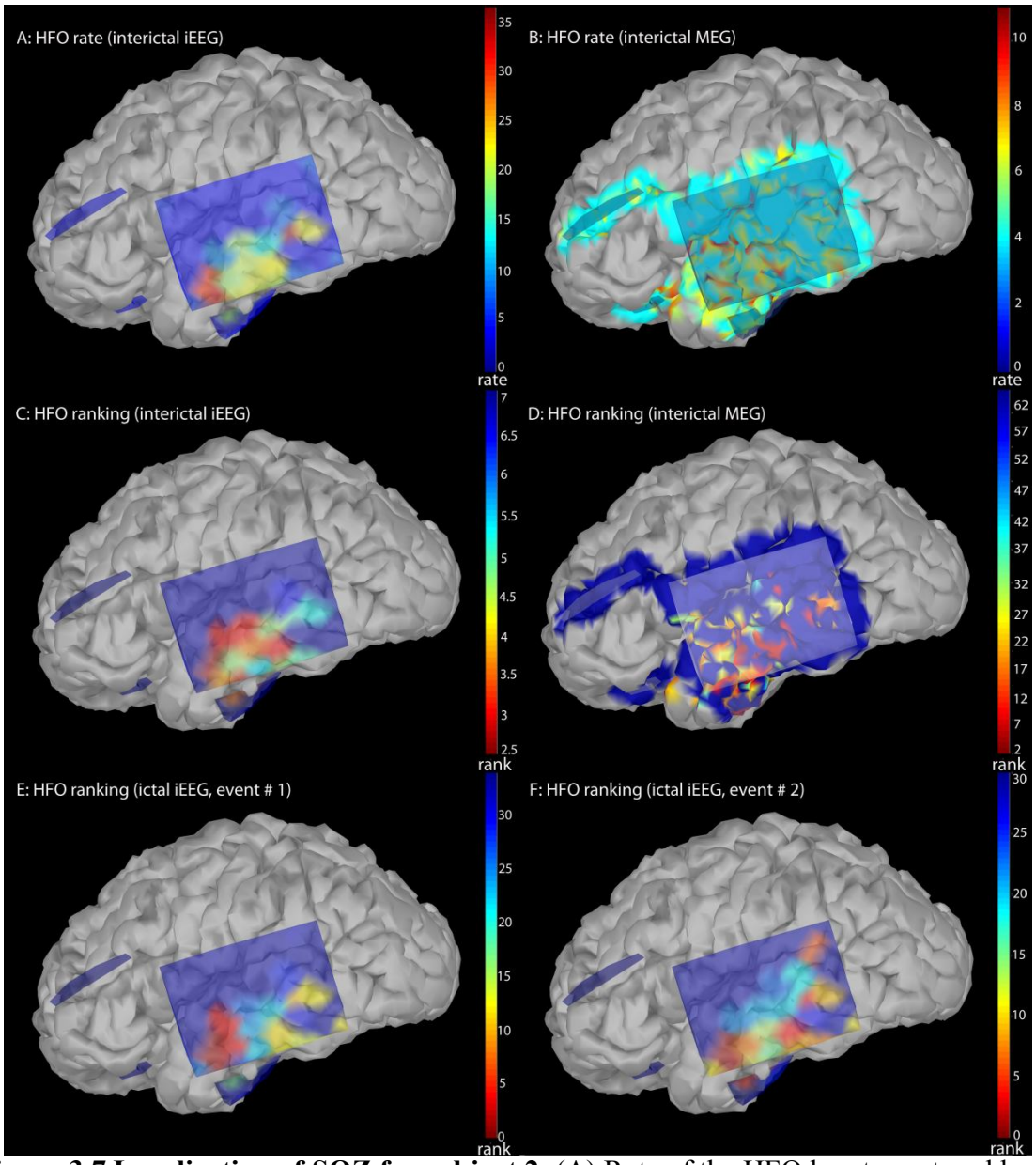

Figure 3.7 Localization of SOZ for subject 2. (A) Rate of the HFO bursts captured by the electrodes during interictal iEEG recording. (B) Rate of HFO bursts detected from each of sources analyzed using the MEG interictal data. (C) Rank of the channels obtained using the same interictal iEEG recording as used to A. Channels with low ranks are classified as SOZ. (D) Rank of the sources obtained using the interictal MEG data. (E) Rank of the channels using the first ictal iEEG recording. (F) Rank of the channels using the second ictal iEEG recording.

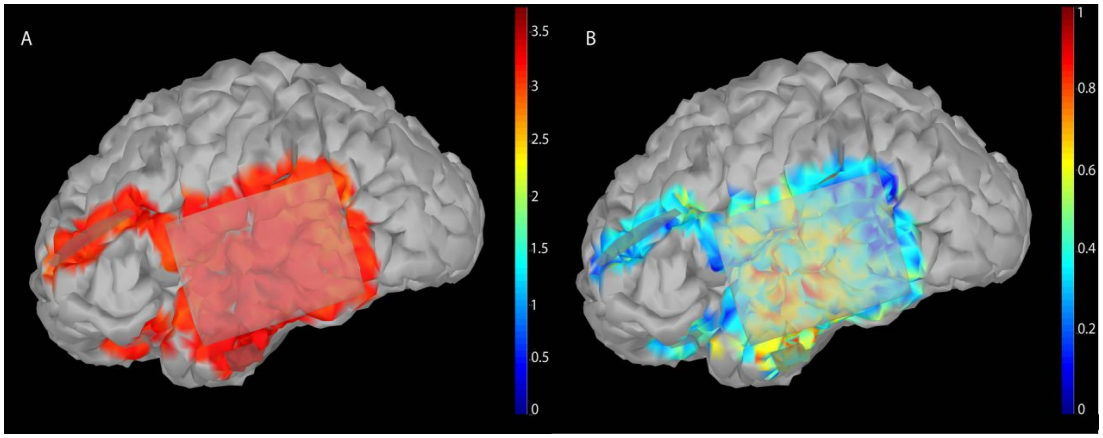

Figure 3.8 Map of MEG spiking indices for subject 2. (A) The spiking indices for all the sources in the non-normalized form. (B) The spiking indices for all the sources in normalized form. The colorbar is normalized to the scale 0-1. The normalized map then localized to similar regions as the rate map or leaders in the rank map.

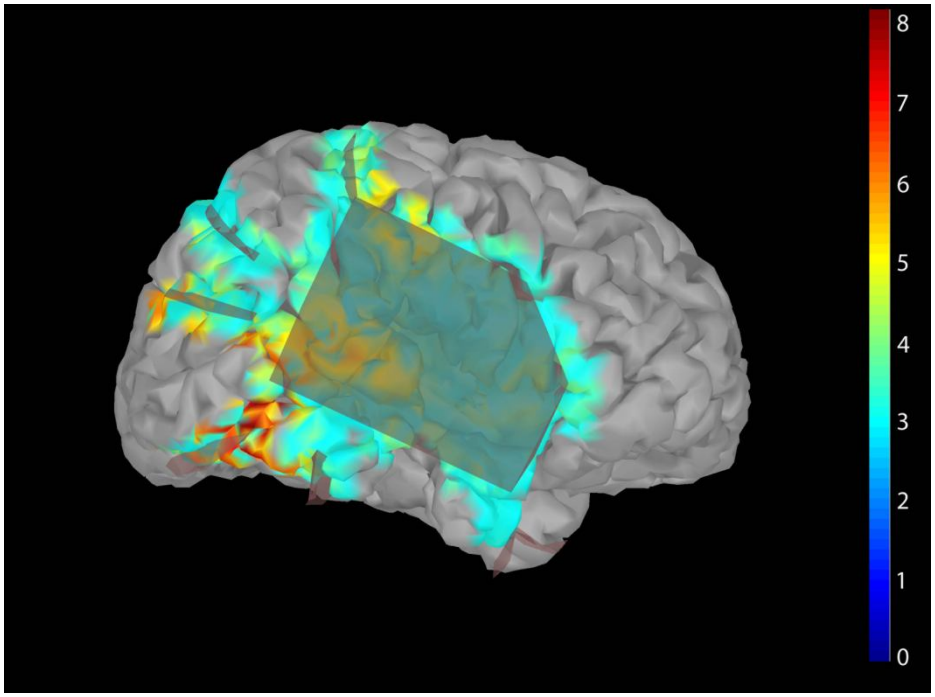

Figure 3.9 Map of MEG spiking indices for subject 3. The spiking index value for all the sources. The regions with maximum values localized to the same regions as the rate or the rank map in Figure 3.10.

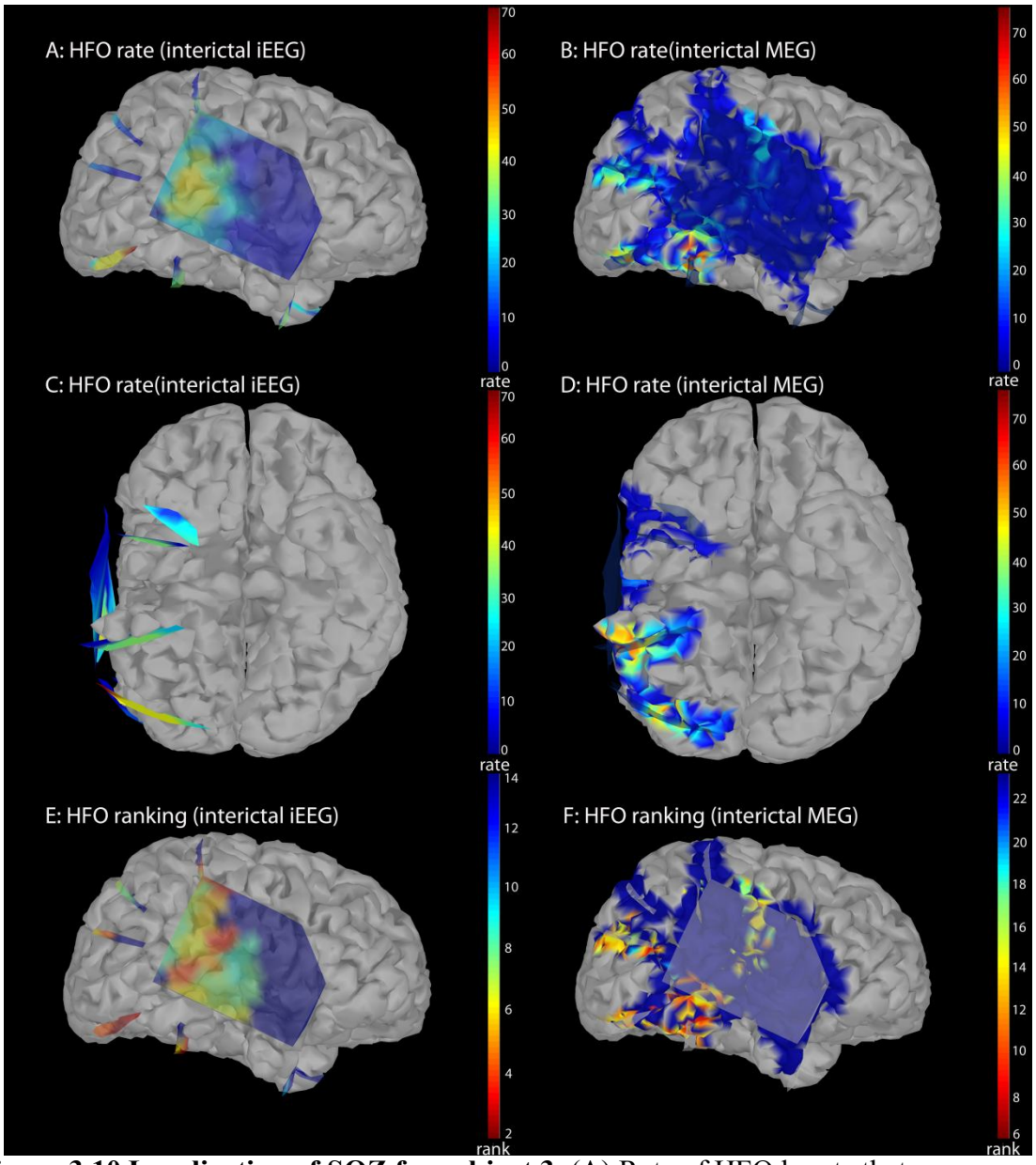

Figure 3.10 Localization of SOZ for subject 3. (A) Rate of HFO bursts that were captured during interictal iEEG recording. (B) Rate of HFO bursts that were captured by the interictal MEG recording. (C) Ventral view of panel A. (D) Ventral view of panel B. (E) Rank of the channels using iEEG interictal recording. (F) Rank of the sources obtained using the interictal MEG data.

4. Discussion

4.1 Comparison Between Wavelet Analysis and Hilbert Transform

The standard procedure for identifying the SOZ is based on visual observation of the recorded data from an expert neurologist. However, identifying the HFOs across large number of channels and across huge volume of data is very tedious and time consuming, even for experienced neurologists. The channels with low-amplitude HFOs can be overlooked when other channels show high-amplitude HFOs. It was essential that we developed an algorithm capable of detecting these HFOs, to ensure better reliability and faster throughput of clinical data analysis. Marking manually these HFOs is also subjected to biasing based on the opinion of the reviewer. An algorithm, in agreement with expert reviewers, would help develop certain benchmarks that would facilitate smooth flow of information during clinical review and across clinicians. The algorithm designed should ideally be much faster than manual observation and produce results that are more reliable.

We tested two methods, the ButIf toolbox that implemented wavelet transforms and the Hilbert transform for detecting HFOs. We simulated HFOs so that we could test the detections generated by the algorithms against ground truth. A large number of signal segments (N=300) with HFOs were simulated and a smooth ROC curve was obtained. True positives, false positives, true negatives and false negatives were determined to compute the sensitivity and specificity of the tested algorithms. We plotted the ROC curve from the sensitivity and the specificity values, which gave a fair idea of how well the algorithms performed.

The ButIf toolbox performed well in terms of sensitivity but performed poorly in terms of specificity. The specificity could be increased with the reduction of maximum number of bump features to be modeled or the pruning value, and by increasing the detection threshold, but there would be reduction of sensitivity. The wavelet analysis transformed a 1-D time domain signal into a 2-D time-frequency map consisting of wavelet coefficients. Increase in dimensionality led to a considerable rise in computational demand. The number of dimensions should ideally be kept to a minimum in order to reduce complexity. The algorithm also involved transfer of data from Matlab to C++ and back, which further increased the computational expenses. The primary reason we opted for another method was mainly due to the computational expenses involved and the run time of the algorithm since it took about 6.5 hrs to complete the ROC analysis. The C++ code was converted into an executable file which acted as a black box. It worked only under the Windows environment. This severely hampered the portability of the algorithm onto multiple operating systems. Multiple simultaneous calls to executable files in Windows were restricted and the workaround involved creating multiple copies of the executable.

Hilbert transform computed the analytic signal and retained the time information. The dimensionality rise involved with the Hilbert transform was minimum (=5), . The magnitude of the Hilbert transformed signal estimated the envelope of the signal. The envelope was accurate if the signal was band-limited to a narrow range and thus the frequency range of interest between 80-300 Hz was divided into five sub-bands. The Hilbert transform was quicker and took about 5 minutes to complete the entire ROC analysis which was a huge gain in time and reduction in complexity. The algorithm

worked in different computer environments, without requiring any change in the code. The matrix of a raw baseline signal was [1 x 2000] and the wavelets transformed this matrix to [76 x 2000] where the number of rows depended on the frequency binning. This was a huge increase in dimensions as compared to the Hilbert transform where the transformed matrix was a [5 x 2000] matrix. The Hilbert transform detected the events with comparable sensitivity as ButIf toolbox but with improved specificity. The area under the curve further justified our decision of opting for the approach based on the Hilbert transform (0.93 as opposed to 0.81 for ButIf).

Our approach could be further refined by determining the amplitude of HFOs using other metrics. Currently, the amplitude of HFOs was determined using the means of the time series obtained from 50 magnetometers. The mean can sometimes be an inaccurate metric especially when the mean of the sensors is zero, which indirectly causes the amplitude of HFO to be zero. Although this might rarely happen, it is still a possibility. An alternative metric could be the root mean square (RMS) value, which is more robust than the mean value. The RMS value incorporates information of the variance and thus increases the robustness in the determination of the amplitude of HFOs.

In the current study we band-pass filtered the data into five frequency intervals (80-124Hz, 125-169 Hz and so on). For the HFOs that had frequency exactly at 124 or 125 Hz, we would expect a reduction in their power due to the frequency binning. Overlapping frequency bins could be employed to facilitate detection of HFOs that lie at the edges of each frequency range. If the overlap is large we might detect repetitive events but since we were considering just one event from a channel at one instant of time, detecting more events would not affect the analysis.

4.2 Parameters for Detecting the SOZ from Physiological Data Using Hilbert Transform

In order to detect the seizure onset zone accurately from physiological data, some parameters needed to be specified by the user that were crucial for the detection of HFOs, and hence the SOZ. One of the parameters was the '*threshold*'. The threshold was used for selecting the events whose amplitude was above the user set threshold. If the value was set very high, events of potential interest would be missed. If it was set to a very low value, there would be too many false positives. For iEEG, we set the threshold value to 5 which was greater than the optimal threshold to enable greater specificity. Further, the SNR for iEEG was high and hence we could afford to raise the threshold without losing important information. For MEG, SNR remained a key issue and with a threshold of 5 events of potential interest were missed and hence the threshold value was set to 4. We computed the length of the detected events and if its length was less than 4 cycles, the event was not considered into the analysis. Parameter '*Min_grp*' determined the minimum number of channels that needed to be present in one group event for it to be considered in the analysis. For iEEG this value was set to five, since there were electrodes in the range of 50 to 100. For MEG, this value was set to 100 since there were greater than 2000 sources for each subject. Parameter '*Per_rem*' determined the minimum number of group events a particular channel/source must be present for it to be considered for analysis. If a channel was present in just one group event and happened to be the leader purely by chance, its rank would be one which would interfere with the ranks of other potential leading channels. The parameter prevented false detections from

gaining significance. For iEEG, the value of Per_rem was set to 20% of total group events, and for MEG the value was set to 10%.

4.3 HFOs as a Potential Biomarker of Seizure Onset Zone

One of the aims of the study was to understand the clinical significance of HFOs in an epileptic network. According to our hypothesis, HFOs could act as a reliable biomarker for determining the SOZ in patients with intractable partial epilepsy. Patients with generalized epilepsy generally have a good control over seizures by means of medication. Surgery is considered as an option for some patients with intractable partial epilepsy. The epileptic spikes during the interictal and ictal states are traditionally used as a standard measure for taking a clinical decision regarding resection of cortex. These epileptic spikes were found to increase after seizure, which suggested that the spikes might be an effect of seizure rather than the cause of seizure genesis (Gotman J, 1989). It was determined by Zijlmans et al., that the rate of HFOs decreased post seizure while the epileptic spikes increased post-seizure. Antiepileptic medications were found to reduce the rate of HFOs while the rate of spikes was overall unaffected.

In our study, the MEG and iEEG data were not acquired simultaneously and hence we could not verify of the simultaneous presence of HFOs in both MEG and iEEG. The data was also collected under different circumstances: iEEG data was collected with the subjects under no influence of medications, and the MEG data was collected with subjects under the influence of medications.

The spikes typical frequency range is 3-4 Hz (Gibbs et al., 1935) and the SOZ was localized using the information available from high frequency oscillations in the 80-

300 Hz range. No information from the spike frequency range was included in the analysis. The detected HFOs present in iEEG and MEG data were able to localize the SOZ from the interictal data for the three subjects that were analyzed, thus strengthening the participation of HFOs in epileptic activity. The regions of the cortex localized by the algorithm as SOZ were verified by an expert neurologist. The study definitely needs to be expanded to include more subjects as a long term goal since the results were very encouraging.

4.4 HFO rate map v/s HFO Rank Map and Relevance of Using MEG Data for SOZ Localization

The HFO rate map is a visual representation of the number of HFOs bursts for channels/sources during the recording. The map representing HFO ranks is a visual representation of the rank of the channels/sources during the group events. HFO rate and rank map are two different metrics and might provide coinciding information. A channel/source might produce a maximum number of bursts but that does not guarantee its temporal precedence over other channels/sources. A SOZ might have fewer bursts, but it might be the leader of the group oscillations on average. For subject 1, the region that produced maximum bursts was not the same as the SOZ. The HFO rate map provides useful information regarding the areas that are bursting frequently, as possible contenders for the SOZ location. The HFO rate map might not be the best way to analyze iEEG data since we have very clean data and HFO ranking can accurately localize the SOZ. But for techniques like MEG, which explores the whole head non-invasively, this metric can be quite useful.

The MEG data does not have as high SNR as iEEG and it is one of the major drawbacks when compared with iEEG. The MEG data was also hampered by the fact that the subjects were under medications and its effect could be seen when we set the threshold to 5. There was hardly any activity in case of MEG above the threshold of 5 as opposed to iEEG where the complete analysis was performed at the threshold of 5. This is in agreement with Zijlmans et al, whose findings showed that the HFO rate and amplitude decreases by medications (Zijlmans et al., 2009). Therefore, we reduced the threshold to 4 for the MEG analysis since sensitivity was a concern. Also, we restricted our analysis to the areas of the cortex under the grid. If we had analyzed the entire cortex, we might have additional regions of interest, but the results could not be compared with iEEG. As we develop sufficient confidence in the MEG results by analyzing results from a larger pool of subjects, we plan to expand the analysis to cover the entire cortex.

iEEG is an invasive procedure and cannot be used as an exploratory procedure, which is where MEG can prove to be very useful. One can use MEG non-invasively and determine the possible SOZ regions. This information could be used to improve the targeting and the placement of subdural electrodes for pre-surgical evaluation. The ranking method using the MEG data also provided good localization of SOZ but the area covered by a single source was very small, as compared to the area covered by the electrode and also there were huge numbers of sources analyzed, which made the ranking method difficult to visualize as there were plenty of sources with the same rank.

4.5 Advantage of Using Interictal over Ictal iEEG Data

We analyzed interictal data from three subjects and ictal data from two subjects. We focused on the propagation pattern of the HFOs that were detected by the algorithm. The channels that led the propagation patterns on average were classified as SOZ. If one visually inspected the data, it clearly seemed that oscillations from one particular region drove other regions towards a bursting oscillatory behavior. During interictal state though, this activity did not lead to a seizure. We may hypothesize that during the interictal state the SOZ experiences bursts of excitation that can potentially entrain the brain to seize, but a certain kind of '*threshold*' is not exceeded and restricts further spread. Once this *'threshold'* is exceeded, a seizure ensues and the epileptic activity propagates to other cortical regions. The SOZ localization using interictal and ictal data showed good concordance for the two subjects. In other words, the SOZ, as identified from HFOs remained the same for interictal or ictal state of the brain.

During the interictal state, only some of the regions were oscillating whereas the rest of the cortex was relatively silent. During the ictal state, there were plenty of regions involved which made the data difficult to analyze. Therefore we restricted our analysis to the first second of the seizure, defined as the ictal onset. Interictal data was therefore easier to analyze since we could extract plenty of information from the multiple group of oscillations that occurred regularly in a particular epileptic patient. The ranks of the channels from interictal data would be much more stable and reliable since there were plenty of group oscillations available from which we could average the ranks. In case of ictal data, there was just one group oscillation that was captured at the ictal onset. The ranks of the channels were thus more likely to show variability since we had no means of

averaging the ranks across many seizures. In a conventional setting, the epileptic patient is monitored for several days under reduced medication. This causes the patient to seize and the ictal data is used for obtaining clinical decision. Typically only a few seizures are captured for this purpose. If we could localize the SOZ accurately by using the interictal data, we would not require such a long invasive procedure which is both risky and uncomfortable to patients. It would also save valuable time of the clinical staff and accuracy regarding the resection would not be compromised either. The fact that the third subject was operated purely on the basis of interictal data also supports our claim that interictal data can, in some cases, be a useful source of information regarding the localization of SOZ. Although the subject had brief auras in the weeks immediately after surgery, the subject has been seizure free since. These results are preliminary and would need further validation across much larger patient groups in order to establish our claim with greater confidence.

4.6 Spiking Index

Spiking index was another metric we proposed to localize regions that burst with high signal amplitudes. It was defined as the ratio of maximum value of the envelope of a particular source during a HFO group event, to the mean of the envelope over the entire recording. It would give us an idea regarding how drastically a source undergoes a change in amplitude during a group event. For subjects 1 and 3, it gave fairly good and straight-forward results that aligned with the results obtained from the rate map. For subject 2, it was not as easy to interpret. The spiking index of subject 2 was trickier since the spike index of all the sources was close in value to one another. This result broadened

our understanding about the implications regarding the spiking index. The fact that the data for subject 2 was silent during the MEG recording could be verified from its HFO rate map, which showed the maximum rate of HFOs as 10 during a 5 minute recording in spite of a threshold of value 4. Hence, every source had spike index values close to one another. For the spiking index method to produce good results reliably, one would need high amplitude HFOs present in the data on a consistent basis. We scaled the spiking indices based on the minimum and maximum values to accommodate the range of 0-1. This enhanced the differences between the sources and made it possible to spread the range of data between different sources. We were still able to localize regions that coincided with the HFO rate and rank map but it was less convincing than for subjects 1 and 3.

4.7 Conclusion

Our study focused on the development of methods that could assist the neurologist in making a clinical decision regarding the localization of the SOZ in cases of partial epilepsy. The data analyzed visually by a neurologist is complex and multi-dimensional. We developed an algorithm with the implementation of Hilbert transform for the detection of the HFOs, and associated metrics, to characterize possible regions involved in the epileptic SOZ. The algorithm reduced the number dimensions to 3 (2-spatial coordinates and 1-amplitude). The accuracy of the detection was consistent across subjects and modalities, although the parameters needed to be adjusted based on the type of data under consideration (iEEG or MEG).

The interictal data provided robust information that was comparable to the ictal data for the localization of SOZ. The HFO rate map identified possible regions that could be the SOZ and the ranking method provided the SOZ that were verified by a neurologist. The spiking index used to analyze the MEG data also localized to similar regions as localized by the rate map.

The HFO rate map and spiking index could prove to be useful for noninvasive MEG analysis since these methods localized regions in and around the SOZ for the three subjects we analyzed. IEEG is not a comprehensive exploratory procedure: the information from HFO rate analysis and spiking index using the MEG data could be used alternatively to better target the placement of implantable electrodes prior to surgery. The number of subjects analyzed was one of the limiting factors of our results, but we feel these results are very encouraging.

4.8 Conversion from MEG Source Data to iEEG Data

The implantable electrodes were used for the collection of iEEG data. The electrodes measured the electrical activity of the brain in terms of voltages. MEG data measured the magnetic field of the brain in terms of Teslas by means of sensors. We, then, solved the inverse problem to obtain the source signals that are currents and expressed in units Amperes.meter (A.m). Although the measured electrical potentials and magnetic fields share the same generators, they express different properties in terms of sensitivity to sources and surrounding tissues. In order to compare the localization results of these two techniques, we explored the possibility to combine their information. Therefore, we attempted to convert the source currents into voltages as seen from a

virtual implantable electrode. In a nutshell, we tried to move the MEG source space to iEEG electrode sensor space, so that the localization results between iEEG and MEG could be compared. There are two types of currents that are responsible for producing the voltages in case of iEEG or the magnetic field as measured by the MEG; the primary current sources and the secondary current sources. A primary current source is the intracellular current that flows from the apical dendrites to the cell soma and basal dendrites. In order for the primary current to flow, the current loop needs to be completed and secondary currents flow extracellularly in the surrounding tissues. Figure 2.12 shows the primary current source, secondary current sources and the magnetic field produced around the primary current source as defined by the right hand thumb rule. Primary current sources are the main sources of interest in terms of detection and localization. For simplicity, we considered only the primary current source in our analysis of iEEG voltage generation. The source currents were converted into voltages based on the following formula:

$$V_0(r) = \frac{1}{4\pi\sigma_0} \int J_p(r'). \frac{r-r'}{||r-r'||^3} dr' \ldots\ldots\ldots\ldots (6)$$

$V_0(r)$: Potential produced at location r due to primary current sources;

σ_0: Unit conductivity (1/Ωm) (makes the units consistent);

r: Voltage at point r;

r': Current flow at location r';

$J_p(r')$: Primary current distribution at location r';

Figure 2.13 demonstrates the location of electrodes and sources along with the orientation and magnitude of the current source.

To illustrate the way the voltages were computed, let us assume there are about 3000 sources that lie under the 100 electrodes that comprised the grids and the strips. We obtained the coordinates of the electrodes and the sources, as shown previously, and

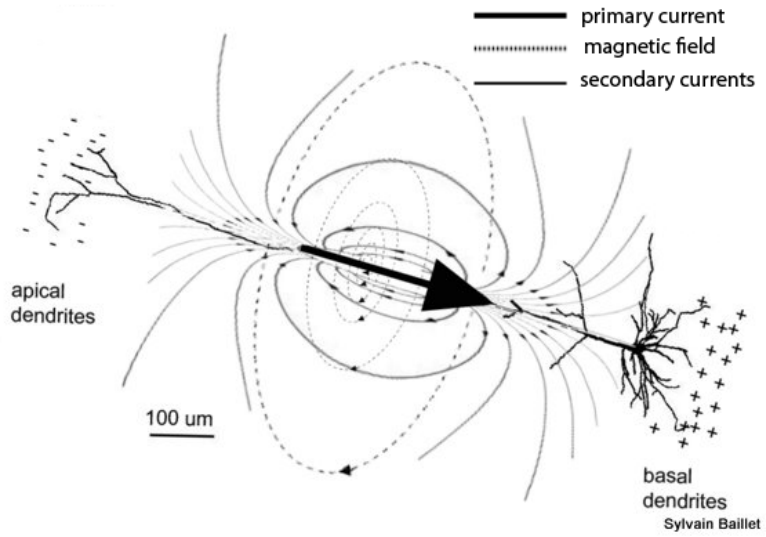

Figure 3.11 Primary current source, secondary current sources and the magnetic field. The darker line with an arrow is the primary current source, the dotted line is the magnetic field produced by the primary current source and the thinner lines looping around the primary current source represents the secondary currents needed to complete the loop that enables the flow of the primary current. Adapted from www.mcw.edu

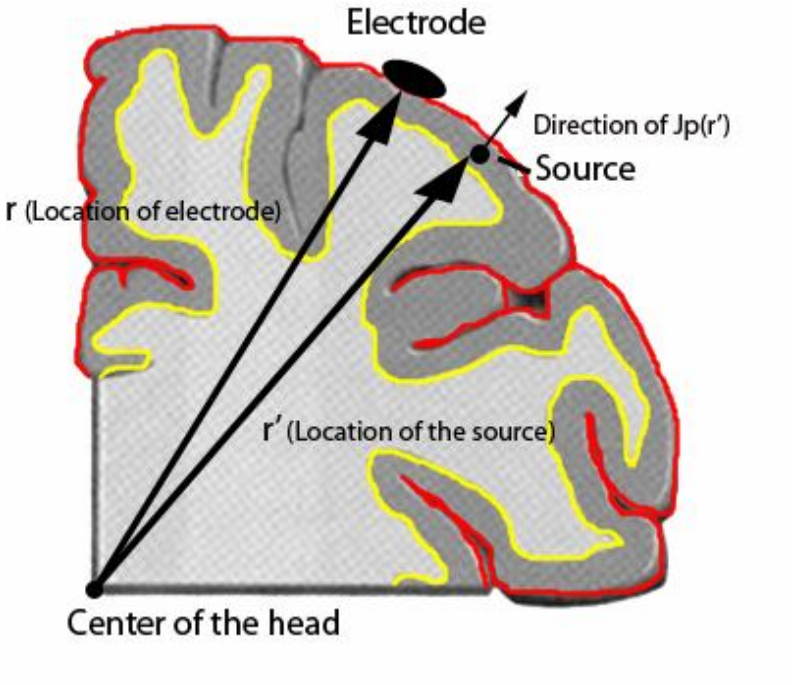

Figure 3.12 Location and orientation of the electrode and source. MEG primary source currents were converted to voltages as measured by an electrode. r and r' were vectors that gave us the position of the electrode and source respectively. J_p (r') was a vector with a magnitude equal to the source current and direction normal to the cortex.

therefore, r and r` were known. Thus the term (r-r`)/||r-r`||^3 could be calculated. We also knew the orientation of the sources since the dipoles were constrained normally to the cortex and we also knew the source currents by solving the MEG inverse problem. If the orientation of a particular source or a dipole was (x,y,z) and the amplitude of the current source at time t was J, then J_p (r`) was (J*x, J*y, J*z). For a particular source, we may calculate the dot product of $J_p$(r`) and (r-r`)/||r-r`||^3. We then computed $\sum_{i=1}^{3000} J_p(r').\frac{r-r\prime}{||r-r'||^3}$ at time t, which yields the primary voltage measured at the electrode position at time t. Similarly, we calculated the primary voltage at the particular electrode at all times and across all electrodes. Thus, a source current matrix of [3000 sources x 5 mins] would yield a [100 electrodes x 5 mins] virtual iEEG voltage array.

5. FUTURE DIRECTIONS

The aim of the study was to localize the SOZ using information from the oscillatory activity at higher frequencies. We were able to localize the SOZ accurately using ictal or interictal iEEG data and interictal MEG data for the three subjects. The algorithm was designed to replicate what a neurologist would conclude from his/her visual observation. The algorithm successfully managed to achieve that. The study focused on the development of methods and the next step would be to focus on its clinical validation at a larger scale. Below are some steps required to improve the methods and to help establish the study clinically.

5.1 Increase the Number of Subjects

The study was performed by analyzing the previously recorded iEEG and MEG data from three subjects. The results regarding the localization of SOZ were encouraging but would the results still hold when the study includes more subjects? The aim would be to expand the study to include more subjects to establish a relatively strong level of confidence. The results based on analysis of large number of subjects would be more reliable and also expand our understanding regarding the significance of HFOs in the epileptic network. With a greater number of subjects analyzed, the user defined

parameters on which the algorithm relies currently could be stabilized to the values that produce the best results on a group average.

Interictal data was able to localize the SOZ accurately for the three subjects. If the results hold for a larger number of subjects, it could have a significant impact in the clinical environment where ictal data is considered as the gold standard.

5.2 Set a Research Protocol

The fact that this study was a post-hoc study gave rise to a number of inconsistencies with respect to the data analyzed. The volume of data analyzed varied with subjects. A specific research protocol could be designed to collect the data as required and to test the algorithm. This would iron out the unnecessary variables involved. The non-normalized spiking index for subject # 2 was not very informative and we concluded it was due to very silent data. The subject during the acquisition of MEG data is under the influence of anti-epileptic medications and this seems to severely affect the rate and amplitude of HFOs. Thus, we had to reduce the threshold for detecting the oscillatory activity. Once a research protocol is established, the MEG data could be collected without the influence of medications on the subjects (inpatient procedure). This would enhance the quality of recorded MEG data and the results could be more conclusive.

5.3 Implement Algorithm to Convert MEG Source Data to iEEG Data

The research is always an ongoing process and there is lot of scope for improvement. One of the future goals is to implement the algorithm that enables to move

from the MEG source space to the iEEG electrode space, which would enable us to merge information from the MEG and iEEG. The algorithm has been developed but the current efforts to yield useful results have been unsuccessful so far.

BIBLIOGRAPHY

Adelson P, Black P, Madsen J, Kramer U, Rockoff M, Riviello J. Use of subdural grids and strip electrodes to identify a seizure focus in children. *Pediatr Neurosurg*; 22(4): 174-80, 1995.

Baillet S, Mosher J, Leahy R. Electromagnetic brain mapping. *IEEE Signal Processing Magazine*; 18(6): 14-30, 2001.

Baule G.M, McFee R. Detection of the magnetic field of the heart. *American Heart Journal*; 66:95-6, 1963.

Behrens E, Zentner J, van Roost D, Hufnagel A, Elger CE, Schramm J. Subdural and depth electrodes in the presurgical evaluation of epilepsy. *Acta Neurochir*; 128(1–4):84-7, 1994.

Blakemore S, Frith U. The Learning Brain: Lessons for Education: A précis. *Developmental Science;* 8(6): 459-471, 2005.

Benson, DF, Blumer, D. Psychiatric aspects of neurologic disease. *New York, Grune & Stratton;* 151-170, 1975.

Bragin A, Engel J Jr, Wilson CL, Fried I, Mathern GW. Hippocampal and entorhinal cortex high-frequency oscillations (100–500 Hz) in human epileptic brain and in kainic acid-treated rats with chronic seizures. *Epilepsia;* 40:127–137, 1999a.

Bragin A, Engel J Jr, Wilson CL, Vizentin E, Mathern GW. Electrophysiologic analysis of a chronic seizure model after unilateral hippocampal KA injection. *Epilepsia*; 40:1210–1221, 1999b.

Bragin A, Wilson CL, Staba RJ, Reddick M, Fried I, Engel J Jr. Interictal high-frequency oscillations (80–500 Hz) in the human epileptic brain: entorhinal cortex. *Ann Neurol;* 52:407–415, 2002b.

Brázdil M, Halámek J, Jurák P, Daniel P, Kuba R, Chrastina J, Novák Z, Rektor I. Interictal high-frequency oscillations indicate seizure onset zone in patients with focal cortical dysplasia. *Epilepsy Research;* 90:28-32, 2010.

Buzsaki G, Horvath Z, Urioste R, Hetke J, Wise K. High frequency network oscillation in the hippocampus. *Science*; 256:1025–1027, 1992.

Buzsaki G. Rhythms of the brain. *Oxford University Press, New York*, 2006.

Cimatti Z, Schwartz D P, Bourdain F, Meunier S, Bleton JP, Vidailhet M. *Brain;* 130:198-205, 2007.

Cramer JA, Fisher R, Ben-Menachem E, French J, Mattson RH. New antiepileptic drugs: comparison of key clinical trials. *Epilepsia*; 40(5):590-600, 1999.

Dale AM, Fischl B, Sereno MI. Cortical surface-based analysis. I. Segmentation and surface reconstruction. *Neuroimage*; 9:179-194, 1999.

Dale AM, Halgren E. Spatiotemporal mapping of brain activity by integration of multiple imaging modalities. *Curr Opin Neurobiol;* 11:202–208. 2001.

De Salles AA, Swartz BE, Lee TT, Delgado-Escueta AV. Subdural recording and electrical stimulation for cortical mapping and induction of usual seizures. *Stereotact Funct Neurosurg*; 62(1–4):226-31, 1994.

Demoment G. Image reconstruction and restoration: Overview of common estimation structures and problems. *IEEE Trans. Acoust. Speech, Signal Processing*; 37:2024-2036, 1989.

Dugundgi J. Envelopes and Pre-envelopes of Real Waveforms. *IRE transactions of Information Theory,* 1958.

Düzel E, Habib R, Schott B, Schoenfeld A, Lobaugh N, McIntosh AR, Scholz M, Heinze HJ. A multivariate, spatiotemporal analysis of electromagnetic time-frequency data of recognition memory. *Neuroimage;* 18:185-197, 2003.

Engel J, Bragin A, Staba R, Mody I. High-frequency oscillations: what is normal and what is not? *Epilepsia;* 50:598–604, 2009.

Fischl B, Sereno MI, Dale AM. Cortical surface-based analysis. II: Inflation, flattening, and a surface-based coordinate system. *Neuroimage;* 9:195-207, 1999.

Fischl B, Salat DH, Busa E, Albert M, Dieterich M, Haselgrove C, van der Kouwe A, Killiany R, Kennedy D, Klaveness S, Montillo A, Makris N, Rosen B, Dale AM. Whole brain segmentation: automated labeling of neuroanatomical structures in the human brain. *Neuron;* 33:341-355, 2002.

Gardner A, Worrell G, Marsh E, Dlugos D, Litt B. Human and automated detection of high-frequency oscillations in clinical intracranial EEG recordings. *Clinical Neurophysiology;* 118:1134–1143, 2007.

Gibbs F, Davis H, Lennox W. The EEG in epilepsy and in conditions of impaired consciousness. *Arch Neurol Psychiat;* 34:1134-48, 1935.

Gotman J, Koffler D. Interictal spiking increases after seizures but does not after decrease in medication. *Electroenceph. Clin. Neurophysiol;* 72:7–15, 1989.

Haas L. Hans Berger (1873-1941), Richard Caton (1842-1926) and electroencephalography. *Journal of Neurology, Neurosurgery & Psychiatry;* 74 (1): 9, 2003.

Ibarz J, Foffani G, Cid E, Inostroza M, Prida L. Emergent Dynamics of Fast Ripples in the Epileptic Hippocampus. *The Journal of Neuroscience;* 30(48): 16249-16261, 2010.

Jacobs J, LeVan P, Chander R, Hall J, Dubeau F, Gotman J. Interictal high-frequency oscillations (80-500 Hz) are an indicator of seizure onset areas independent of spikes in the human epileptic brain. *Epilepsia*; 49:1893-907, 2008.

Jacobs J, Zelmann R, Jirsch J, Chander R, Châtillon C, Dubeau F, Gotman J. High frequency oscillations (80–500 Hz) in the preictal period in patients with focal seizures. *Epilepsia*; 50(7):1780–1792. 2009.

Kahane P, Landré E, Minotti L, Francione S, Ryvlin P. The Bancaud and Talairach view on the epileptogenic zone: a working hypothesis. *Epileptic Disorders;* 2:16-26, 2006.

Kwan P, Sills GJ, Brodie MJ. The mechanisms of action of commonly used antiepileptic drugs. *Pharmacol Ther*; 90:21–34. 2001.

Lachaux J, Rudrauf D, Kahane P. Intracranial EEG and human brain mapping, *J Physiol;* 97:613–628, 2003.

LaViolette PS, Rand SD, Raghavan M, Ellingson BM, Schmainda KM, Mueller WM. 3D Visualization of Subdural Electrodes for Presurgical Planning. *Neurosurgery*; In Press, 2010.

Leahy R, Mosher J, Spencer M, Huang M, Lewine J. A study of dipole localization accuracy for MEG and EEG using a human skull phantom. *Electroencephalogr. Clin. Neurophysiol;* 107:159-173. 1998.

Li X, Yao X, Fox J, Jefferys J. Interaction dynamics of neuronal oscillations analysed using wavelet transforms. *Journal of Neuroscience Methods;* 160:178-185, 2007.

Luders H, Awad I, Burgess R, Wyllie E, Van Ness P. Subdural electrodes in the presurgical evaluation for surgery of epilepsy. *Epilepsy Res Suppl*; 5:147-56, 1992.

Murakami S, Okada Y. Contributions of principal neocortical neurons to magnetoencephalography and electroencephalography signals. *J Physiol*; 575:925-936, 2006.

Murre, JM, Sturdy, DP. The connectivity of the brain: multi-level quantitative analysis. *Biological cybernetics;* 73(6):529–45, 1995.

Niedermeyer E., da Silva F. Electroencephalography: Basic Principles, Clinical Applications, and Related Fields. *Lippincot Williams & Wilkins*, 2004

Parent A, Carpenter MB. Human neuroanatomy. *Williams and Wilkins, Baltimore,* 1995.

Pfurtscheller G, Cooper R. Frequency dependence of the transmission of the EEG from cortex to scalp. *Electroenceph. clin. Neurophysiol;* 38:93–96, 1975.

Quesney LF, Cendes F, Olivier A, Dubeau F, Andermann F. Intracranial electroencephalographic investigation in frontal lobe epilepsy. *Adv Neurol*; 66:243-58, 1995.

Saladin K. Human Anatomy**.** *McGraw Hill*, 2007.

Sekihara K, Takeuchi F, Kuriki S, Koizumi H. Reduction of brain noise influence in evoked neuromagnetic source localization using noise spatial correlation. *Phys. Med. Biol;* 39,937–946, 1994.

Sekihara K, Abramham-Fuchs K, Stefan H, Hllstrandt E. Suppression of background brain activity influence in localizing epileptic spike sources from biomagnetic measurements. *Brain Topogr;* 8:323–328, 1996.

Staba RJ, Wilson CL, Bragin A, Fried I, Engel J Jr. Quantitative analysis of high-frequency oscillations (80–500 Hz) recorded in human epileptic hippocampus and entorhinal cortex. *J Neurophysiol*; 88:1743–1752, 2002a.

Staba RJ, Wilson CL, Bragin A, Jhung D, Fried I, Engel J Jr. High-frequency oscillations recorded in human medial temporal lobe during sleep. *Ann Neurol*; 56:108–115, 2004.

Stuss DT, Gow CA, Hetherington CR . "No longer Gage": frontal lobe dysfunction and emotional changes. *J Consult Clin Psychol;* 60**:**349–359, 1992.

Tallon-Baudry C, Bertrand O, Delpuech C, Pernier J. Stimulus specificity of phase-locked and non-phase-locked 40 Hz visual responses in human. *Journal of Neuroscience;* 16:4240-4249, 1996.

Tikhonov A, Arsenin V. Solutions to Ill-Posed Problems. *Winston, Washington D.C*, 1977.

Vialatte F, Martin C, Dubois R, Haddad J, Quenet B, Gervais R, Dreyfus G. A Machine Learning Approach to the Analysis of Time-Frequency Maps, and Its Application to Neural Dynamics. *Neural Networks*; 20:194-209, 2007.

Vialatte F, Solé-Casals J, Cichocki A. EEG windowed statistical wavelet scoring for evaluation and discrimination of muscular artifacts. *Physiological Measurements*; 29(12):1435-1452, 2008.

Vialatte F, Solé-Casals J, Dauwels J, Maurice M, Cichocki A. Bump time-frequency toolbox: a toolbox for time-frequency oscillatory bursts extraction in electrophysiological signals. *BMC Neuroscience*; 10:46, 2009.

von Economo, C. The Cytoarchitectonics of the Human Cerebral Cortex. *Oxford University Press*, 1929.

Wennberg R, Quesney F, Olivier A, Rasmussen T. Electrocorticography and outcome in frontal lobe epilepsy. *Electroencephalogr Clin Neurophysiol*; 106(4):357-68, 1998.

Ylinen A, Bragin A, Nadasdy Z, Jando G, Szabo I, Sik A, Buzsaki G. Sharp wave-associated high-frequency oscillation (200 Hz) in the intact hippocampus: network and intracellular mechanisms. *J Neurosci;* 15:30–46, 1995.

Zaccariotti VA, Pannek HW, Holthausen H, Oppel F. Evaluation with subdural plates in children and adolescents. *Neurol Res*; 21(5):463-74, 1999.

Zijlmans M, Jacobs J, Zelmann R, Dubeau F, Gotman J. High-frequency oscillations mirror disease activity in patients with epilepsy. *Neurology;* 72:979–986, 2009.